CHEMISTRY OF MATERIALS
Cite This: Chem. Mater. 2018, 30, 6259−6276
Article
pubs.acs.org/cm

Structure, Chemistry, and Charge Transfer Resistance of the Interface between $Li_7La_3Zr_2O_{12}$ Electrolyte and $LiCoO_2$ Cathode

Gulin Vardar,[†,‡,△] William J. Bowman,[†,‡] Qiyang Lu,[†,§] Jiayue Wang,[†,‡] Richard J. Chater,[∥] Ainara Aguadero,[∥] Rachel Seibert,[⊥] Jeff Terry,[⊥] Adrian Hunt,[#] Iradwikanari Waluyo,[#] Dillon D. Fong,[¶] Angelique Jarry,[□,○] Ethan J. Crumlin,[○] Sondra L. Hellstrom,[▽] Yet-Ming Chiang,[§] and Bilge Yildiz*[,†,‡,§]

[†]Laboratory for Electrochemical Interfaces, Department of Nuclear Science and Engineering, Massachusetts Institute of Technology, Cambridge, Massachusetts 02139, United States
[‡]Department of Nuclear Science and Engineering, Massachusetts Institute of Technology, Cambridge, Massachusetts 02139, United States
[§]Department of Materials Science and Engineering, Massachusetts Institute of Technology, Cambridge, Massachusetts 02139, United States
[∥]Department of Materials, Imperial College of Science, London SW7 2AZ, U.K.
[⊥]Department of Physics, Illinois Institute of Technology, Chicago, Illinois 60616, United States
[#]National Synchrotron Light Source II, Brookhaven National Laboratory, Upton, New York 11973, United States
[¶]Advanced Photon Source, Argonne National Laboratory, Lemont, Illinois 60439, United States
[□]Department of Chemistry and Biochemistry, University of Maryland, College Park, Maryland 20742, United States
[○]Advanced Light Source, Lawrence Berkeley National Laboratory, Berkeley, California 94720, United States
[▽]Bosch Research and Technology Center, Sunnyvale, California 94085, United States

Supporting Information

ABSTRACT: All-solid-state batteries promise significant safety and energy density advantages over liquid-electrolyte batteries. The interface between the cathode and the solid electrolyte is an important contributor to charge transfer resistance. Strong bonding of solid oxide electrolytes and cathodes requires sintering at elevated temperatures. Knowledge of the temperature dependence of the composition and charge transfer properties of this interface is important for determining the ideal sintering conditions. To understand the interfacial decomposition processes and their onset temperatures, model systems of $LiCoO_2$ (LCO) thin films deposited on cubic Al-doped $Li_7La_3Zr_2O_{12}$ (LLZO) pellets were studied as a function of temperature using interface-sensitive techniques. X-ray photoelectron spectroscopy, secondary ion mass spectroscopy, and energy-dispersive X-ray spectroscopy data indicated significant cation interdiffusion and structural changes starting at temperatures as low as 300 °C. $La_2Zr_2O_7$ and Li_2CO_3 were identified as decomposition products after annealing at 500 °C by synchrotron X-ray diffraction. X-ray absorption spectroscopy results indicate the presence of also $LaCoO_3$ in addition to $La_2Zr_2O_7$ and Li_2CO_3. On the basis of electrochemical impedance spectroscopy and depth profiling of the Li distribution upon potentiostatic hold experiments on symmetric LCO|LLZO|LCO cells, the interfaces exhibited significantly increased impedance, up to 8 times that of the as-deposited samples after annealing at 500 °C. Our results indicate that lower-temperature processing conditions, shorter annealing time scales, and CO_2-free environments are desirable for obtaining ceramic cathodelelectrolyte interfaces that enable fast Li transfer and high capacity.

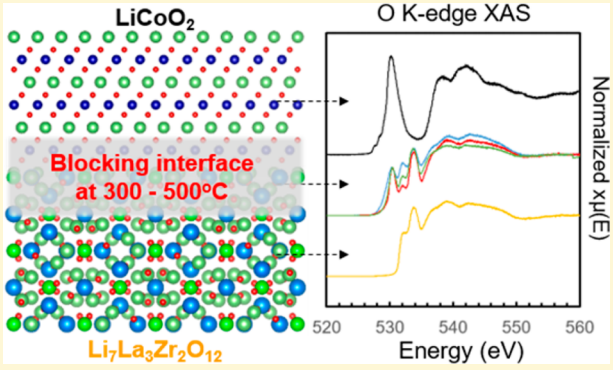

INTRODUCTION

One of the most exciting prospects of solid electrolytes is the possibility of using Li metal as the anode, which would greatly increase the gravimetric energy density over intercalation anodes.[1−6] A number of solid electrolytes with conductivities

Received: April 25, 2018
Revised: July 25, 2018
Published: July 25, 2018

DOI: 10.1021/acs.chemmater.8b01713
Chem. Mater. 2018, 30, 6259−6276

close to that of liquid Li-conducting electrolytes have been reported.[7−13] $Li_7La_3Zr_2O_{12}$ (LLZO) is a promising solid electrolyte due to its relatively high conductivity (in cubic phase, up to ~10^{-3} mS/cm), high chemical stability against Li metal, and large electrochemical window (>5 V vs Li/Li^+).[9,14−20] Recent studies have identified the electrodel electrolyte interface as the main source of high resistance in solid state batteries, thereby limiting their power density.[21−29] While there have been sustained efforts to study Li^+ conductivity in the bulk of solid electrolytes,[9] the kinetics of Li^+ transfer at the electrodelelectrolyte interfaces remains underexplored. Systematic and extensive studies on the chemical composition of these interfaces as a function of well-defined thermal and electrochemical conditions are needed to identify suitable synthesis conditions that form effective and durable interfaces.

Specifically for the LLZO electrolyte, the reaction layer at the Li|LLZO interface was recently identified, and ways to eliminate it were demonstrated.[30−35] The large resistance at the Li metal and LLZO interface was found to be due to the presence of a Li_2CO_3 interfacial layer that forms upon exposure of LLZO to ambient atmosphere prior to deposition of the Li anode. Those studies have shown that the elimination of the Li_2CO_3 layer, either by polishing in inert atmosphere,[27] by annealing in argon gas,[36,37] or by deposition of a lithiated interface coating,[31,35,38] can both reduce the interfacial impedance and increase the critical current density at which Li dendrites form and propagate.[29−32,34−42] Although these advances have been promising for the electrolytelanode interface, the cathodelelectrolyte interface was and still is a large barrier. For example, infiltrating this interface with a liquid electrolyte was necessary to realize a full battery system with a reasonable current density.[38,43,44]

The interface between the solid electrolyte and cathode is a key contributor to impedance in solid-state batteries,[28,45,46] and thus, we believe this interface currently hinders the advancement of solid state batteries. Especially given that most cathodes are oxides, their use with ceramic solid electrolytes may necessitate elevated temperatures to densify and form strongly bonded interfaces with each other. However, these temperatures can facilitate interdiffusion and secondary phase formation that are detrimental to battery performance. Creating a strong contact between oxide cathodes and LLZO while preserving good electrochemical properties therefore remains as a significant challenge.[47] Several experiments have shown that depositing $LiCoO_2$ (LCO) cathode on LLZO above 500 °C yields a good physical bond, but cross-diffusion and decomposition can occur during deposition.[48−50] The use of interlayers between LCO and LLZO may minimize detrimental reactions, but operational batteries using this approach have exhibited limited battery cycling performance.[22,51,52] Another approach that has shown promise is the use of polymer interlayers for mechanical compliance.[53,54] Due to the low conductivity of the polymer interlayers, however, liquid electrolyte penetration of the polymer was necessary to yield a low interfacial impedance.[55]

Experimental probes sensitive to the onset of detrimental phase formation at such buried interfaces are scarce. Previous studies on the cathode|LLZO interface reactivity relied on XRD on mixed powder bulk specimens to identify secondary phases.[47,50,52,56,57] However, the detection limit for bulk XRD is too low to probe the onset of secondary phase formation at an electrochemical interface. Even the formation of a ~10 nm-thick insulating interface can be detrimental to charge transfer but would not be detectable using XRD on bulk powders. The ability to detect the onset of detrimental reactions at the interface of LLZO with oxide cathodes is important for identifying the appropriate synthesis and operating conditions for these ceramic−ceramic interfaces. Studies using more interface-sensitive techniques such as cross-sectional transmission electron microscopy (TEM) or scanning TEM (STEM) are present.[24] Kim et al.[49] suggested the presence of La_2CoO_4 at the interface between a thin-film of LCO deposited at 663 °C onto LLZO. Another study showed that annealing the LCO|LLZO interface at 700 °C induced diffusion of Al (a dopant for cubic LLZO) from LLZO into LCO.[47] This resulted in a cubic-to-tetragonal LLZO phase transition and reduced the Li-ion conductivity of LLZO near the interface.[47] However, no secondary phases were reported, and the findings of these two experimental studies are not consistent with each other.

The thermodynamic instabilities between different cathode materials and LLZO have also been studied computationally.[56,58−60] The decomposition products between LLZO and the cathode materials were predicted to be temperature and voltage dependent.[56,58,60] Miara et al. have found that a driving force exists at the LCO|LLZO interface for the system to decompose and form secondary phases such as La_2O_3, $La_2Zr_2O_7$, and Li_2CoO_3.[58] The decomposition pathways that have been proposed by these computational works have provided much needed insight, but experimental validation is necessary, and any discrepancies should be understood. For example, the previously reported experimental results mentioned above are not consistent with the computational predictions. Furthermore, the reported computational studies largely ignored the existence of CO_2 in the sintering environment (typically air), and any potential presence of Li_2CO_3 is missing.

Here, we conducted a detailed structural and chemical study of the interface between thin, well-defined films of LCO cathode and LLZO electrolyte as a function of temperature, using both *ex situ* and *in situ* interface-sensitive experimental probes. LCO was chosen as the cathode material due to its high electrochemical potential (4.2 V vs Li/Li^+) and its simplicity, as it contains only one transition metal cation that could react with LLZO. We observed decomposition of the LCO|LLZO interface with depth profiling tools, X-ray diffraction, and X-ray absorption spectroscopy. Furthermore, we showed that the chemical transformation of the annealed system degrades charge transfer kinetics significantly at the heterointerface. Importantly, we found that the interface decomposition can be onset at temperatures as low as 300 °C with a detrimental impact on the interface charge transfer resistance. The findings of this work identify desirable processing guidelines, in particular lower-temperature processing conditions, shorter annealing time scales, and CO_2-free environments in the sintering of ceramic cathode−electrolyte interfaces.

Approach and Experimental Methods. Our approach involved a large array of complementary characterization techniques to confirm the interface chemistry and its effect on the charge transfer kinetics. First, to confirm the formation of a smooth and continuous LCO|LLZO interface, the thickness of the LCO layer and the initial phases present, scanning electron microscopy (SEM), X-ray diffraction (XRD), X-ray reflectivity (XRR), and TEM were utilized. Second, composition profiles

DOI: 10.1021/acs.chemmater.8b01713
Chem. Mater. 2018, 30, 6259−6276

obtained by X-ray photoelectron spectroscopy (XPS) and secondary ion mass spectroscopy (SIMS) corroborated each other on the elemental diffusion at the interface. However, these measurements of the compositional depth profile are destructive because of the ion sputtering used in each and thus can induce artifacts. Third, to confirm the elemental mixing and depth profiles in a nondestructive way, STEM energy-dispersive X-ray spectroscopy (EDX), hard X-ray photoelectron spectroscopy (HAXPES), and fluorescence mode X-ray absorption spectroscopy (XAS) were also used. The results from all methods agree that there is significant temperature-induced elemental intermixing at the interface of LCO|LLZO starting with temperatures as low as 300 °C. Furthermore, because the annealing temperatures being studied in this work target the onset of interface reactions and thus are not high enough to crystallize secondary phases fully, conventional characterization methods such as XRD are not suitable to detect secondary phases. Therefore, it was necessary to use spectroscopy methods such as extended X-ray absorption fine structure spectroscopy (EXAFS) and XAS to study the formation of noncrystalline secondary phases. Lastly, potentiostatic hold, electrochemical impedance measurements, and depth profiling of Li by XPS were necessary to reveal the detrimental effect of annealing on the Li transfer kinetics at the interface.

Thin film cathode layers deposited on LLZO electrolyte pellets were employed in this study. Dense thin film cathode layers make an ideal model system because the cathode|electrolyte interface can be accessed by different techniques, including depth profiling by ion sputtering with XPS and SIMS as well as nondestructive depth profiling by HAXPES and electron yield mode XAS. LCO thin films of 20−500 nm thickness were fabricated in this work by radio frequency sputtering onto sintered and polished LLZO pellets.

The as-deposited LCO layers were characterized by SEM, XRD, and XRR (Figure S1). For XRR, LCO was deposited onto single-crystal sapphire substrates to confirm the quality and to calibrate thickness of the deposited films. The morphology of the LCO|LLZO interface in the as-deposited state and after annealing at 500 °C was investigated by cross-sectional TEM. To investigate cation diffusion across the LCO|LLZO interface, several elemental profiling tools were utilized. We used XPS depth profiling in conjunction with Ar^+ ion sputtering to identify the elemental distributions for Co, Li, O, La, Zr and C across the LCO|LLZO interface for a 20 nm LCO layer. Similarly, SIMS depth profiling in conjunction with Ga^+ ion sputtering was used to profile Co, La, Li, and O across the LCO|LLZO interface. Because the Ga^+ ion sputtering removed more material per given time than Ar^+ ion sputtering, a thicker LCO layer of 100 nm was studied with SIMS to observe the LCO|LLZO interface. EDX was also used on the cross-sectional TEM samples to probe the Co, La, and Zr distributions across the interface. These depth profiling tools reveal how the composition of the LCO|LLZO interface evolves as a function of annealing conditions.

Depth profiling by XPS and SIMS necessitates removal of the top layer of the sample by ion beam sputtering. This process can itself induce cation intermixing or preferential sputtering and introduce uncertainties into the information being collected. To negate such potential uncertainties, HAXPES experiments were performed with LCO layers of various thicknesses. HAXPES is a unique, nondestructive tool that allows for data collection at depths up to 30 nm into the sample at X-ray energies of 10 keV.[61] By changing the data collection angle or by changing the thickness of the films, it is possible to collect X-ray photoelectron information as a function of depth, making the results more or less sensitive to the buried interface for comparative purposes.[62]

To identify the effect of annealing temperature on the electronic structure of the LCO|LLZO interface, XAS measurements were performed on LCO films of various thickness on LLZO. These results provide information on the oxidation state and fine structure of the different elements. The collection mode of the XAS measurements determines the sample configuration. For the total or partial fluorescence yield (TFY or PFY) mode, the data is bulk sensitive. For XAS measurements performed in fluorescence mode, the thickness of the LCO film was varied from 20 to 460 nm so that the measurements would be more or less interface sensitive, respectively. The detection depth of the partial electron yield (PEY) mode is on the same order as that of XPS. For *in situ* XAS measurements in PEY mode, 20 nm LCO films were used to determine whether the reaction at the LCO|LLZO interface propagates through the LCO films.

Previous studies used XRD to detect secondary phases in mixed cathode and electrolyte powders.[47,56,63] However, to form secondary phases that are detectable by tube-based XRD, high annealing temperatures (>700 °C) are needed to crystallize the compounds and form sufficient volume fractions. Here, we exploit synchrotron X-ray diffraction to probe a 20 nm LCO film on LLZO before and after annealing. The high intensity of synchrotron radiation was needed to detect possible secondary phases at the interface of this small-volume sample.

EXAFS is a powerful XAS technique that gives information on electron scattering events around the probed element. One advantage of EXAFS over XRD is that EXAFS does not need long-range order for being able to probe the local atomic arrangements. EXAFS analysis was performed at the Co K-edge, La L_3-edge, and Zr K-edge to understand the effect of annealing on the fine structure of these cations. Although EXAFS in TFY is a bulk-sensitive method, it is possible to probe the interface by changing the thickness of the LCO films. For example, because Co is only present in the LCO film, changes to Co fine structure at the interface due to annealing are more apparent for thinner LCO films (20 nm) on LLZO.

Evolution of the interface with annealing temperature affects the charge transfer resistance of the battery. Electrochemical testing was undertaken to understand the effect of annealing on Li transport properties through the LCO|LLZO interface. For this purpose, symmetric LCO|LLZO|LCO cells with Au current collectors were fabricated, and both electrochemical impedance spectroscopy (EIS) and potentiostatic-hold measurements were performed. EIS measurements were performed on LLZO and on LCO|LLZO|LCO to discern impedances associated with bulk conduction in LLZO and with Li-transfer across the LCO|LLZO interfaces before and after annealing. Such symmetric cells are ideal for deducing the LCO|LLZO interface charge transfer resistance by EIS. Using the same cell configurations, potentiostatic-hold experiments were performed at 3 V for 1 h, before and after annealing at 500 °C, to test whether Li can flow through the cell upon sintering-induced formation of detrimental interface chemistries. The equilibrium potential for this symmetric cell to start with is 0 V, and we do not expect further Li intercalation into the LCO

DOI: 10.1021/acs.chemmater.8b01713
Chem. Mater. 2018, 30, 6259−6276

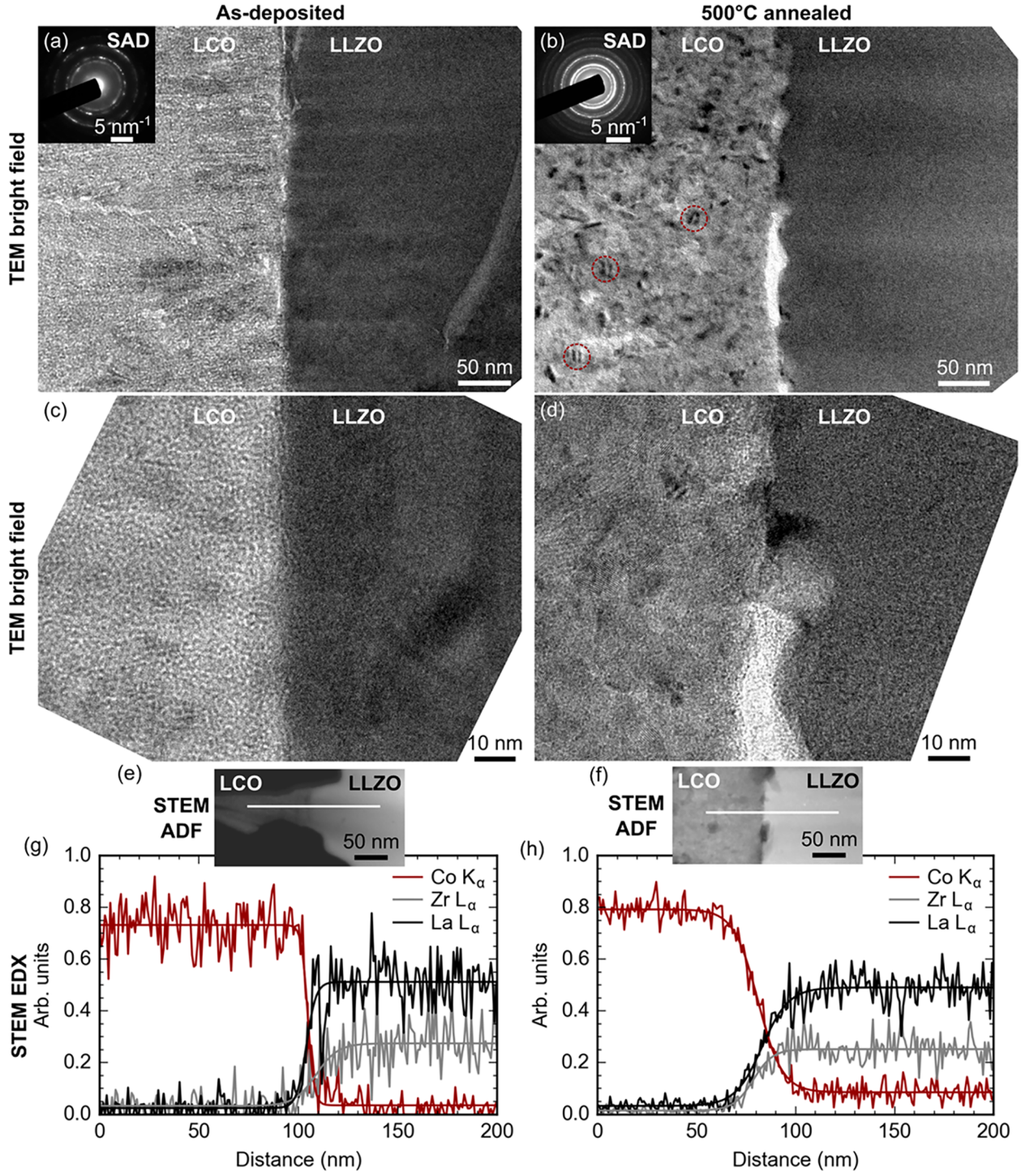

Figure 1. TEM and STEM analysis of interface morphology and elemental distribution for LCO|LLZO samples with 460 nm LCO deposited onto LLZO in the as-deposited state (a, c, e, and g) and after annealing at 500 °C (b, d, f, and h). (a and b) Low-resolution TEM bright field images with inset diffraction patterns acquired in LCO phase. (c and d) High-resolution TEM bright field images showing interface morphology. (e and f) STEM annular dark field images with EDX line scan paths highlighted with horizontal lines. (g and h) Representative STEM EDX elemental profiles; signal intensities are normalized to the total X-ray signal intensity (see eq 1 in the Experimental Procedures).

layers. XPS depth profiling was used to measure the Li profiles on both sides of the LCO|LLZO|LCO samples after potentiostatic hold to determine how much the Li transfer was impeded across the interface upon annealing. Upon potentiostatic hold, delithiation on one LCO and Li plating on the opposite LCO was found, indicating that Li was able to flow through the cell. After annealing at 500 °C, there was no discernible Li transport across the LCO|LLZO interfaces.

RESULTS

A. Compositional Profiles across LCO|LLZO Interfaces. We measured evolution of the chemical composition across the interface by both local and lateral-averaging probes.

DOI: 10.1021/acs.chemmater.8b01713
Chem. Mater. 2018, 30, 6259−6276

While the former based on TEM gives detailed and local visualization, the latter based on XPS and SIMS provides a globally averaged understanding; they together give a more complete picture of chemical evolution.

In Figure 1, we present TEM images of the LCO|LLZO interface and elemental distributions across the interface as measured by STEM-EDX spectroscopy for both the as-deposited state and after annealing at 500 °C. The low magnification images in Figures 1(a) and (b) reveal that the interface in the as-deposited sample was mostly continuous and generally uniform. The interface after annealing at 500 °C exhibited regions of apparent porosity, visible as bright regions in Figures 1(b) and (d) separated by regions of interfacial continuity. The interface morphologies, as measured by high-resolution TEM (HRTEM), before and after annealing are shown in Figures 1(c) and (d). The apparent decrease in the LCO−LLZO contact area after annealing was accompanied by a morphological change in the LCO. The LCO exhibits well-defined regions of strong diffraction contrast approximately 10−20 nm in diameter, e.g., those circled in Figure 1(b). These regions are attributed to nanocrystallites, which are directly observable as lattice fringe contrast in Figure 1(d). The presence of nanocrystalline LCO was also evidenced with selected area electron diffraction (SAED), as shown in the inset of Figure 1(b). The SAED patterns obtained from the "bulk" of LCO film (~200 nm from the interface) exhibit narrow, nearly continuous concentric rings of spots due to Bragg diffraction from randomly oriented nanocrystallites. The SAED patterns from the as-deposited LCO film (see inset in Figure 1(a)) do not exhibit continuous rings but rather well-separated Bragg spots attributed to a lower volume fraction of the crystalline phase when compared to the annealed LCO layer. The diffraction data presented here were indexed to LCO, although it was not possible to differentiate between its polymorphs. Nanobeam diffraction patterns acquired from the bright regions of the annealed interface in Figure 1(b) indicate the absence of crystallinity; as discussed below, these interface regions are believed to be voids due to Li_2CO_3 decomposition based on STEM EDX measurements.

The elemental distribution at the LCO|LLZO interfaces was measured using STEM EDX to investigate the influence of annealing on cation interdiffusion. Figures 1(e) and (f) present STEM annular dark field (ADF) images of the LCO|LLZO interfaces in the as-deposited state and after annealing at 500 °C. In STEM ADF images, the intensity is approximately proportional to the squared mean atomic number of the material, so the apparent voids visible as bright regions in Figures 1(b) and (d) appear as dark regions in Figures 1(e) and (f). Figures 1(g) and (h) present representative elemental distribution profiles for Co, Zr, and La measured in the as-deposited and annealed specimens through the LCO|LLZO interface. For quantitative comparison of cation interdiffusion behavior, analysis was performed in regions of the annealed interface where there is direct LCO|LLZO contact. The profiles were fit to logistic curves to estimate the interface chemical width. The interface widths determined from Co K_α, Zr L_α, and La L_α broadened from 14.2 ± 10.4 to 27.2 ± 5.9 nm, from 16.7 ± 9.8 to 22.2 ± 2.1 nm, and from 15.1 ± 9.1 to 28.7 ± 7.7 nm, respectively, upon annealing the as-deposited sample at 500 °C. These are mean values calculated from four measurements with errors indicating one standard deviation. Using STEM ADF imaging, voids within the LCO are visible in addition to voids at the LCO−LLZO interface, as shown by Figure 1(f). Figure S2 presents STEM EDX analysis of the LCO−LLZO interface voids and LCO voids. It is possible that these apparent voids observed in the TEM specimen are the result of Li_2CO_3 decomposition during Ga^+ ion beam milling used for TEM specimen preparation. Li_2CO_3 has been shown to exhibit high sensitivity to electron beam irradiation effects with the authors attributing decomposition to knock-on damage, ionization, and heating effects[64] which, to varying degrees, are also expected during Ga^+ beam irradiation.

Figure 2 shows depth profiles obtained by XPS and ion sputtering on 20 nm LCO films on LLZO in the as-deposited and annealed conditions. Co was confined mostly to the first 40 min of sputtering in the as-deposited film. After the films were annealed, the Co profile spread out over a longer period of sputtering, indicating that the Co diffused from the LCO film into the LLZO layer, forming a reaction zone. The maximum atomic percentage of Co in the as-deposited sample was 30%, whereas this value dropped to 20% after annealing at 300 °C and to 10% after 500 °C. The Co/Li ratios of these samples are shown in Figure 2(d). The peak of the Co/Li ratio decreased and moved toward the LLZO substrate as a function of annealing.

Importantly, the carbon profile also changed significantly with annealing; the C signal rose near the surface and penetrated deeper into the sample. This indicated the formation of Li_2CO_3, as shown by examination of the C 1s X-ray photoelectron peaks in Figure 3. The C 1s XPS profile showed that there was adventitious carbon (285 eV) on the surface as well as Li_2CO_3 (290 eV).[65] The shape of the C 1s peaks before any sputtering agreed well with previous literature.[27,36,37,66] After Ar ion sputtering, the adventitious carbon signal was completely removed. However, the C 1s signature from Li_2CO_3 was still present below the surface within the LCO and LLZO zones of the annealed sample. The C 1s signature associated with Li_2CO_3 decreased as the sputtering progressed well into the bulk of LLZO.

Figure 4 shows depth profiles obtained by SIMS and Ga ion sputtering on LCO|LLZO samples for a 100 nm LCO in the as-deposited state (a) and after annealing at 300 °C (b). Li, La, and Co signals were normalized to the O signal. Similar to the XPS depth profiles in Figure 2, the Co/O signal spread out over a larger sputtering depth within the annealed sample. To understand cation interdiffusion, we focus on the region where the Co/O signal crosses the La/O signal. For the as-deposited sample, the Co/O intensity ratio starts a sharp decline before the La/O signal reaches 10^{-1}, which is the value of La/O ratio in the LLZO pellet. After annealing at 300 °C, the Co/O signal shows a slower decline before the La/O signal stabilizes at the LLZO value of 10^{-1}. This change in the shape of the Co/O and La/O profiles indicate cation intermixing takes place at the interface, consistent with the XPS depth profiling shown above.

Figure 5(a) shows the Co/Li ratios calculated from HAXPES data obtained on LCO|LLZO samples with a 20 nm deposited LCO layer as a function of emission angle. The lower emission angles correspond to more surface sensitive measurements, and the higher emission angles probe deeper into the sample (see Figure S3). For the as-deposited sample, there was a sharp decline in the Co/Li ratio as the emission angle is changed from 70° to 80°, indicating that in the 80° configuration the data originates from both the LLZO substrate as well as the LCO layer. After annealing at 300 and 500 °C, the Co/Li ratio decreased at lower emission angles and increased for higher emission angles. This result

DOI: 10.1021/acs.chemmater.8b01713
Chem. Mater. 2018, 30, 6259−6276

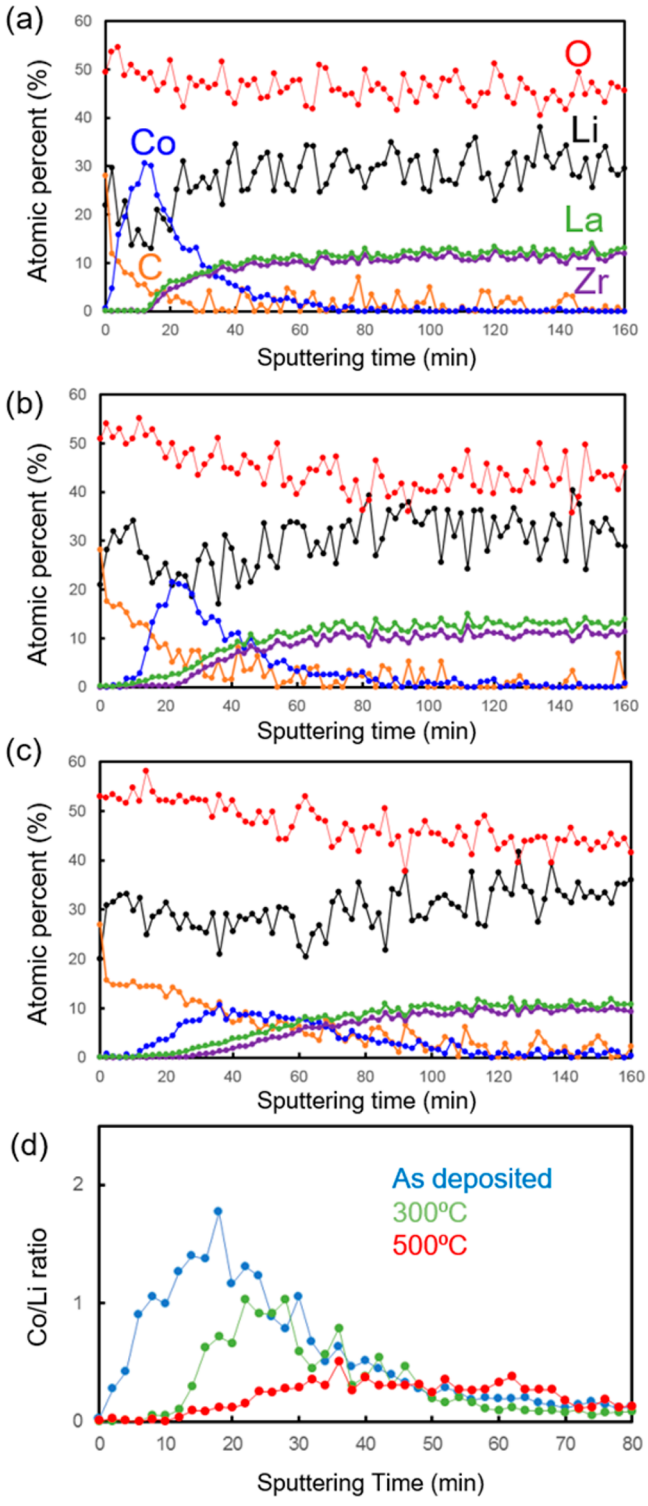

Figure 2. Depth profiles of Li, Co, O, La, Zr, and C for LCO|LLZO samples with a 20 nm deposited LCO layer, obtained by X-ray photoelectron spectroscopy and ion-sputtering in the (a) as-deposited state, (b) after annealing at 300 °C, and (c) after annealing at 500 °C. (d) Co/Li ratios obtained by Co 2p and Li 1s X-ray photoelectron spectroscopy data for the same samples shown in (a), (b), and (c).

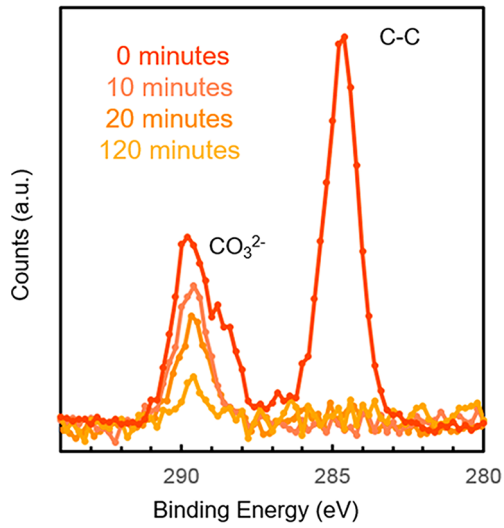

Figure 3. C 1s X-ray photoelectron spectra on an LCO|LLZO sample with a 20 nm deposited LCO layer after annealing at 500 °C and after 0, 10, 20, and 120 min of Ar ion sputtering.

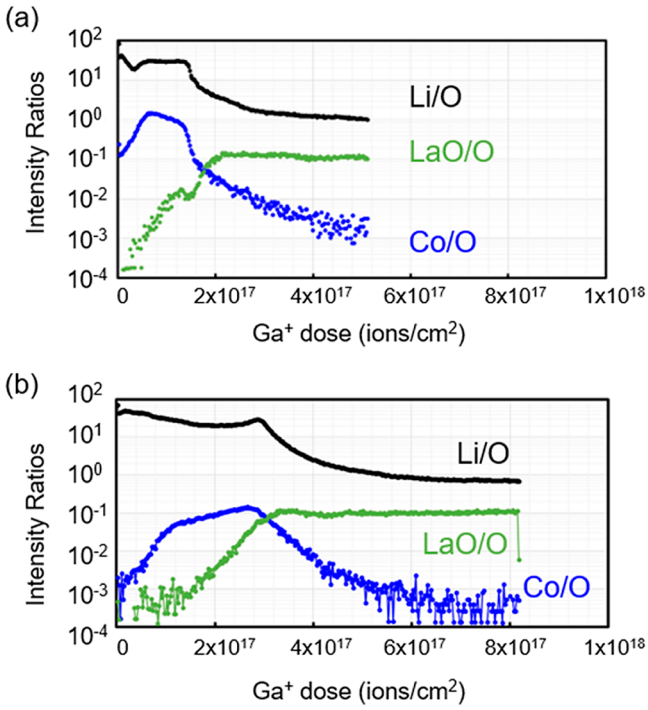

Figure 4. Depth profiles of Li, La, and Co for LCO|LLZO samples with a 100 nm deposited LCO layer obtained by secondary ion mass spectroscopy and ion-sputtering in the (a) as-deposited state and (b) after annealing at 300 °C.

shows that Co penetrates deeper into the sample after annealing at these temperatures. The change in the Co/Li ratio after annealing agrees with the depth profiles measured by XPS and SIMS discussed above. In addition, the C 1s peak associated with Li_2CO_3 is also increased with annealing near the surface (Figure S4), which agrees with the XPS profiling results discussed above.

Figure 5(b) shows the La/O ratios calculated from HAXPES measurements on a reference LLZO sample and on the LCO|LLZO samples in the as-deposited state and after annealing at 500 °C. For the LLZO reference, the measured La/O ratio was close to 0.25, which is in agreement with the La/O ratio expected in the bulk LLZO pellet. For the 20 nm LCO film on LLZO, there was no La signal detected at either angle, indicating that the detection depth of HAXPES at 10 keV was less than 20 nm and that the 20 nm-thick film continuously

DOI: 10.1021/acs.chemmater.8b01713
Chem. Mater. 2018, 30, 6259−6276

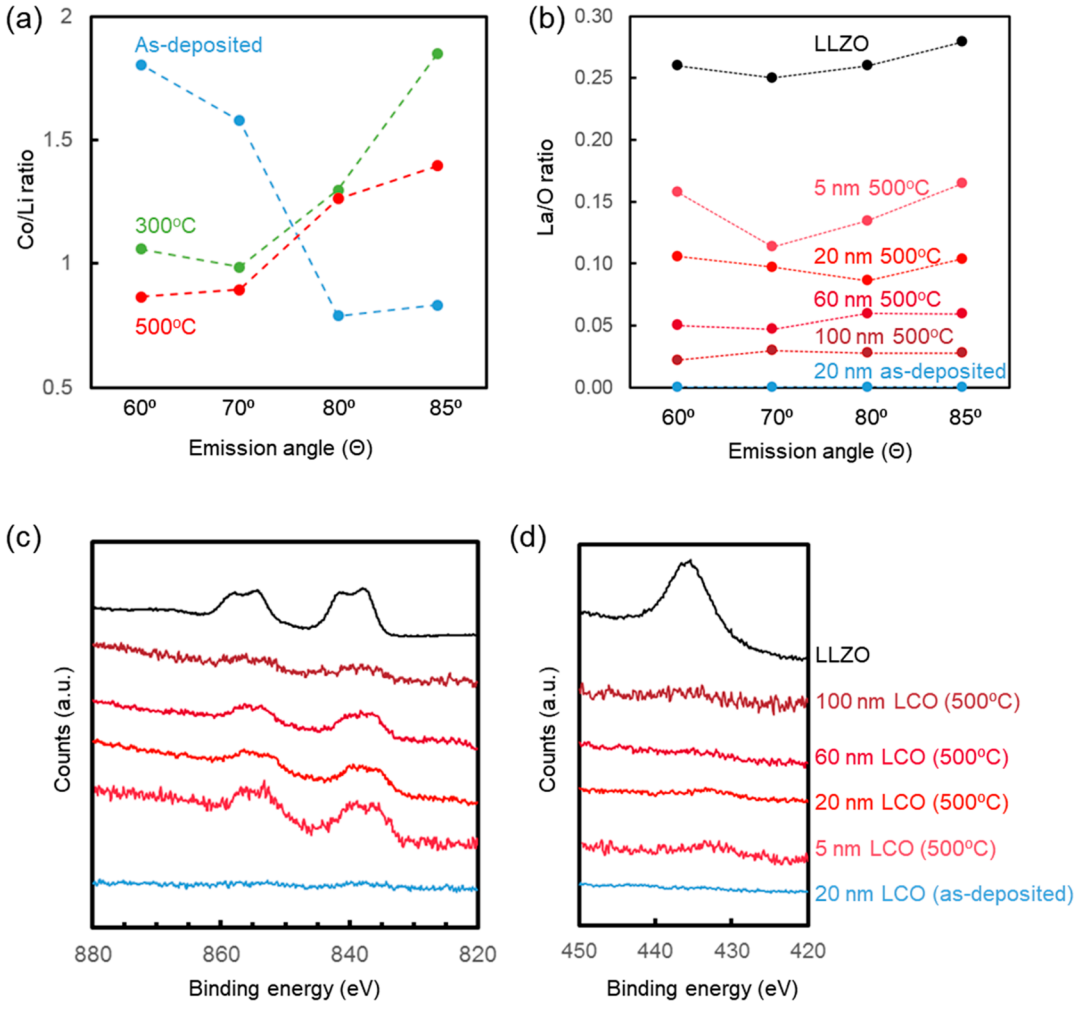

Figure 5. (a) Co/Li ratio obtained by Co 3d and Li 1s hard X-ray photoelectron spectroscopy as a function of emission angle for the LCO|LLZO samples with a 20 nm deposited LCO layer in the as-deposited state and after annealing at 300 and 500 °C. (b) La/O ratios obtained by La 3d and O 1s hard X-ray photoelectron spectroscopy as a function of emission angle for a LLZO pellet and LCO|LLZO samples with 20 nm deposited LCO layer in the as-deposited state and with 5, 20, 60, 100 nm deposited LCO layers after annealing at 500 °C. (c) La 3d and (d) Zr 3s photoelectron emission peaks measured by hard X-ray photoelectron spectroscopy at 85° emission angle for a LLZO pellet and LCO|LLZO samples with 20 nm deposited LCO layer in the as-deposited state and with 5, 20, 60, 100 nm deposited LCO layers after annealing at 500 °C.

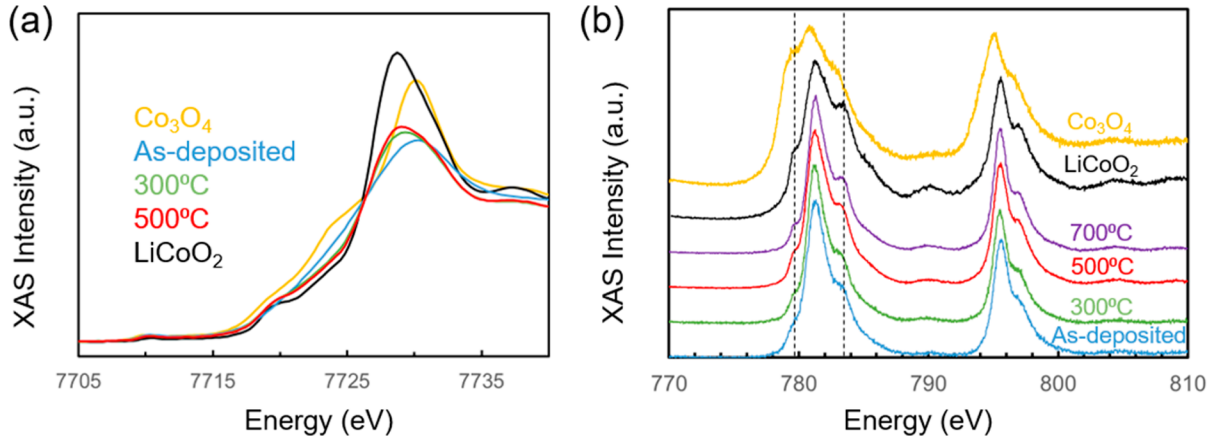

Figure 6. (a) Co K-edge X-ray absorption spectra (total fluorescence yield mode) for Co_3O_4, $LiCoO_2$, and LCO|LLZO samples with a 460 nm deposited LCO layer in the as-deposited state and after annealing at 300 and 500 °C. (b) Co L_3-edge X-ray absorption spectroscopy data (partial fluorescence yield mode) for Co_3O_4, $LiCoO_2$, and LCO|LLZO samples with a 460 nm deposited LCO layer in the as-deposited state and after annealing at 300, 500, and 700 °C.

DOI: 10.1021/acs.chemmater.8b01713
Chem. Mater. 2018, 30, 6259−6276

covered the LLZO surface. After annealing the LCO|LLZO samples at 500 °C, La signal was detected at the surface of the films. To understand La diffusion to the surface of the LCO layers, several LCO layers of varying thicknesses were measured after annealing at 500 °C. The La/O ratios decreased as the LCO film thickness increased from 5 to 100 nm, indicating that the La diffused across the LCO layer at elevated temperatures. From these data, the reaction zone between the LCO and LLZO was on the order of 100 nm after annealing at 500 °C. To confirm that the La 3d signal detection was not due to the LCO film dewetting from the LLZO surface, the Zr 3d signal was compared to the La signal (Figures 5(c) and (d)). Significant La signal was detected from 60 and 100 nm-thick LCO layers annealed at 500 °C, which was not the case for Zr. This comparison shows that the La diffuses further into the reaction zone than Zr.

B. Oxidation State Obtained by X-ray Absorption Spectroscopy. Figure 6(a) shows Co K-edge XAS data collected in TFY mode from 460 nm-thick LCO|LLZO samples in the as-deposited state and after annealing at 300 and 500 °C, as well as from reference $LiCoO_2$ and Co_3O_4 powders. All XAS spectra were normalized to equal 1 in intensity in the postedge region, and the edge energy was taken to be at an XAS intensity of 0.5. In fluorescence mode, X-rays penetrate through the entire LCO layer; therefore, signal from La and Zr can be observed clearly in the spectra (Figure S5). The La and Zr edge energies do not shift with annealing; however, the annealing process induces an increase in the Co oxidation state as the Co K-edge shifts to higher energies. To quantify the change in the oxidation state, XAS data were collected from $LiCoO_2$ (Co^{3+}) and Co_3O_4 ($Co^{2.7+}$) reference samples. The shift in the edge energy can be interpolated linearly with respect to the change in the oxidation state of Co.[67,68] With this approach, the as-deposited 460 nm LCO film corresponds to $Co^{2.8+}$ (consistent with a Li-rich starting point) and LCO films after annealing at 300 and 500 °C correspond to $Co^{2.9+}$.

In Figure 6(b), we present *ex situ* Co L_3-edge XAS data collected in PFY mode from 460 nm LCO films on LLZO in the as-deposited state and after annealing at 300, 500, and 700 °C, as well as reference measurements on $LiCoO_2$ and Co_3O_4 powders. The shoulder on the low-energy side of the Co L_3-edge (~780 eV) indicates more reduced states for Co, whereas the shoulder on the high-energy side (~784 eV) indicates more oxidized states. Compared with the Co L_3-edge XAS spectra for $LiCoO_2$ and Co_3O_4, the low-energy shoulder is more prominent in the Co_3O_4 spectrum, whereas the high-energy shoulder is more prominent for $LiCoO_2$. For the LCO films that have been annealed, the contribution from the low-energy shoulder decreases with annealing temperature. This change in the L_3-edge peak shape indicates an increase in the Co oxidation state with annealing and agrees with the Co K-edge XAS measurements. In addition to the shoulder/peak ratio, the features in the Co L_3-edge are sharper for the annealed samples, which indicates an increase in the crystal field strength. An increase in the crystallization of the LCO layer agrees with the TEM and EXAFS results. XAS measurements at the La L_3- and Zr K-edges (Figure S5) reveal no change with annealing.

Figure 7 depicts O K-edge XAS data for 60 nm LCO films on LLZO in the as-deposited state after annealing at 300 and 500 °C and reference measurements on LCO and LLZO. Because these measurements were taken in fluorescence mode,

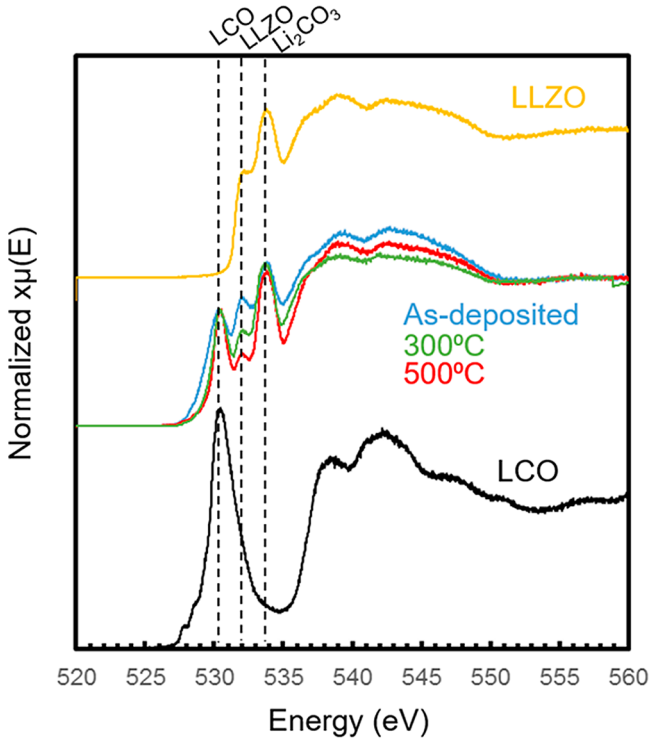

Figure 7. O K-edge X-ray absorption spectroscopy data (partial fluorescence yield mode) for LLZO, LCO, and 60 nm-thick LCO film on LLZO in the as-deposited state after annealing at 300 and 500 °C.

it was possible to detect LLZO through a 60 nm film of LCO. The reference measurements on LCO and LLZO were useful in identifying the three peaks in the O K-edge spectra for the 60 nm LCO films. LCO has an O K-edge peak at 530.2 eV.[69] The LLZO pellet was exposed to atmosphere and therefore exhibits a peak for Li_2CO_3 at 534 eV, and the O K-edge peak associated with LLZO can be observed at 532.1 eV as a shoulder to the Li_2CO_3 peak.[39] The O K-edge XAS data for the 60 nm LCO films are overlaid to see the effect of annealing. The Li_2CO_3 peak was present for all the 60 nm LCO films and did not increase in intensity significantly with annealing. Similarly, the LCO peak remained at the same intensity with the annealing steps. However, the peak associated with LLZO decreased in intensity compared to the LCO and Li_2CO_3, which could indicate the decomposition of the LLZO near the interface with LCO. The O K-edge data were collected also on an annealed 460 nm LCO film on LLZO and show a similar decrease in LLZO peak intensity compared to LCO and Li_2CO_3 (see Figure S6).

C. Decomposition of the Li_2CO_3 on LLZO by Heating in Oxygen. To better understand the nature of Li_2CO_3 decomposition at elevated temperatures, we measured O K-edge X-ray absorption and C 1s X-ray photoelectron spectra for a LLZO pellet as a function of temperature (Figure 8); the data were measured *in situ* while heating the specimens in O_2 gas. The atmosphere during the heating experiments was 30 mTorr of pure O_2 to avoid further formation of Li_2CO_3. Because the XAS spectra were collected in partial electron yield mode, the detection depths of the O K-edge measurements were similar to those for the C 1s XPS spectra (~3 nm).[67] The room temperature LLZO sample exhibited adventitious carbon (C−C, 284.8 eV binding energy) and Li_2CO_3 species (C═O, 288.8 eV binding energy), as can be seen in the C 1s spectra.

DOI: 10.1021/acs.chemmater.8b01713
Chem. Mater. 2018, 30, 6259−6276

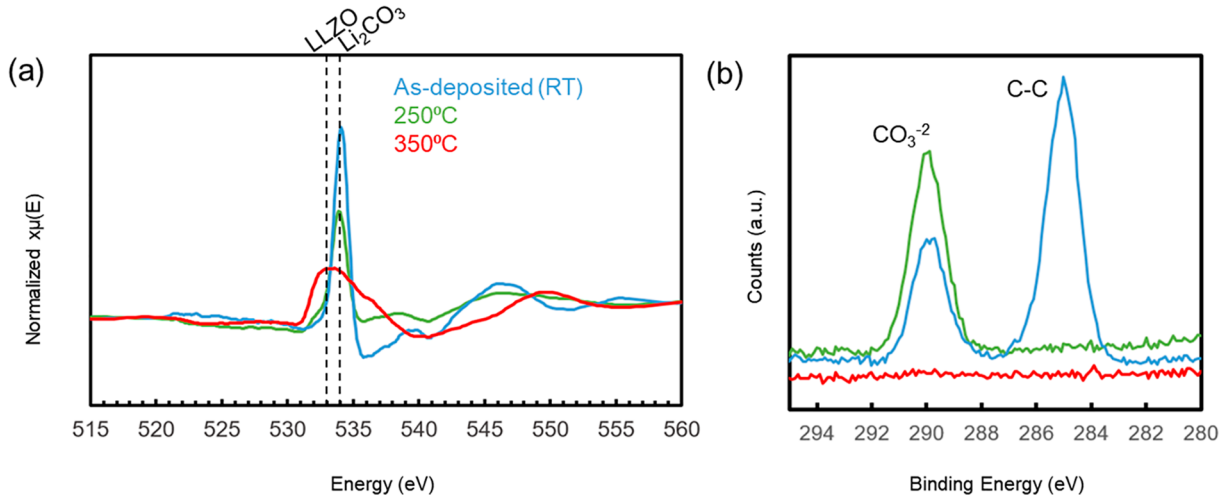

Figure 8. (a) O K-edge X-ray absorption spectroscopy data (in partial electron yield mode) and (b) C 1s X-ray photoelectron spectroscopy spectra for a LLZO pellet measured in situ at room temperature, 250 °C, and 350 °C in 30 mTorr pure O_2.

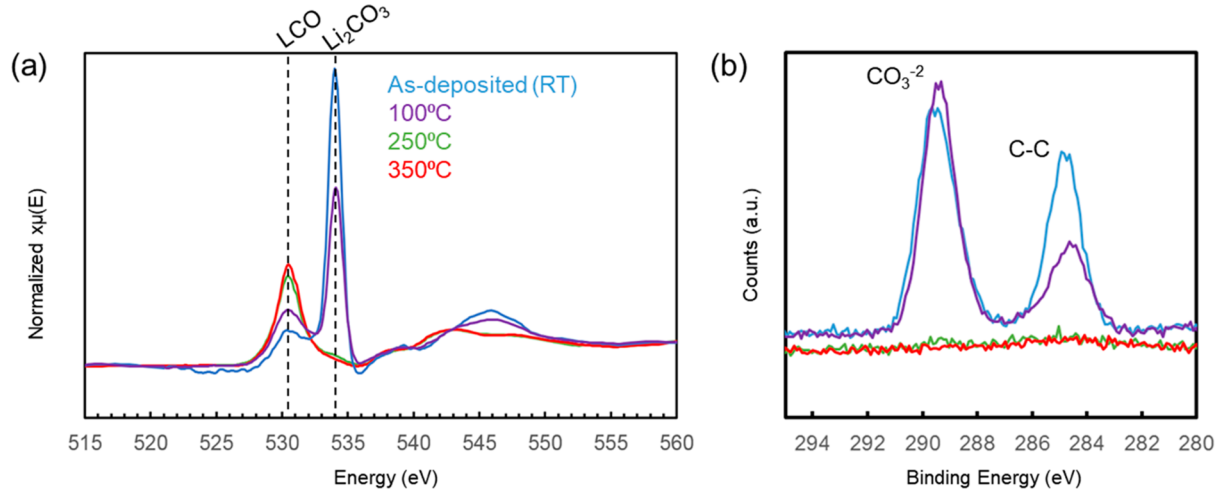

Figure 9. (a) O K-edge X-ray absorption spectra (in partial electron yield mode) and (b) C 1s X-ray photoelectron spectra for a LCO|LLZO sample with a 20 nm deposited LCO layer, measured in situ at room temperature, 100, 250, and 350 °C in 30 mTorr of pure O_2.

The O K-edge data were in agreement with the C 1s XPS spectra and shows a large presence of lithium carbonate (534 eV) at room temperature. After the sample was heated to 250 °C, the adventitious carbon disappeared, but the C 1s peak associated with carbonate persisted on the LLZO pellet. When the sample was heated to 350 °C, all C species were removed from the surface, according to the C 1s XPS spectrum. Furthermore, the O K-edge spectrum at 350 °C illustrated that the carbonate peak disappeared and a broad peak associated with LLZO appeared, indicating that the carbonate layer on top of the LLZO pellet was removed completely. *In situ* XPS spectra for all other regions are presented in Figure S7. Figure S7(b) shows the Li 1s spectra after the carbonate layer is removed and indicates that the LLZO layer under the carbonate layer is Li-poor. Furthermore, the La/Zr ratio (calculated from the La 4d and Zr 3d peaks in Figure S7) is ~1.5 after Li_2CO_3 evaporation, consistent with the La/Zr stoichiometry in LLZO. This indicates that the interface was still LLZO (also consistent with the LLZO peak remaining in the O K-edge XAS in Figure 8) and has not decomposed into $La_2Zr_2O_7$ upon removal of Li_2CO_3.

Figure 9 shows the O K-edge spectra and C 1s photoelectron spectra for a 20 nm LCO film on LLZO as a function of temperature measured *in situ*. According to the C 1s spectra, the as-deposited film exhibited Li_2CO_3 species as well as adventitious carbon. The O K-edge spectra confirmed the presence of Li_2CO_3 species on the surface and in the LCO layer. When the sample was heated to 100 °C, the adventitious carbon C 1s XPS peak diminished and the O K-edge intensity showed decreased Li_2CO_3 and increased LCO signal. When the sample was heated to 250 °C, the C 1s peaks completely disappear, indicating that all carbon species were removed from the surface. Data at the O K-edge confirmed removal of the carbonate species, as the peak at 534 eV photon energy was absent. After heating the sample to 350 °C, the spectra at the C 1s and the O K-edge remained unchanged compared to the spectra measured at 250 °C. *In situ* XPS spectra for all other regions is presented in Figure S8. Figure S8(d) shows that a weak La 4d peak could be detected at the surface of the 20 nm LCO films at 350 °C; however, Zr could not be detected, which agrees with the *ex situ* HAXPES results. Therefore, the reaction zone between LCO and LLZO is less than 20 nm at 250 °C but close to 20 nm at 350 °C.

DOI: 10.1021/acs.chemmater.8b01713
Chem. Mater. 2018, 30, 6259−6276

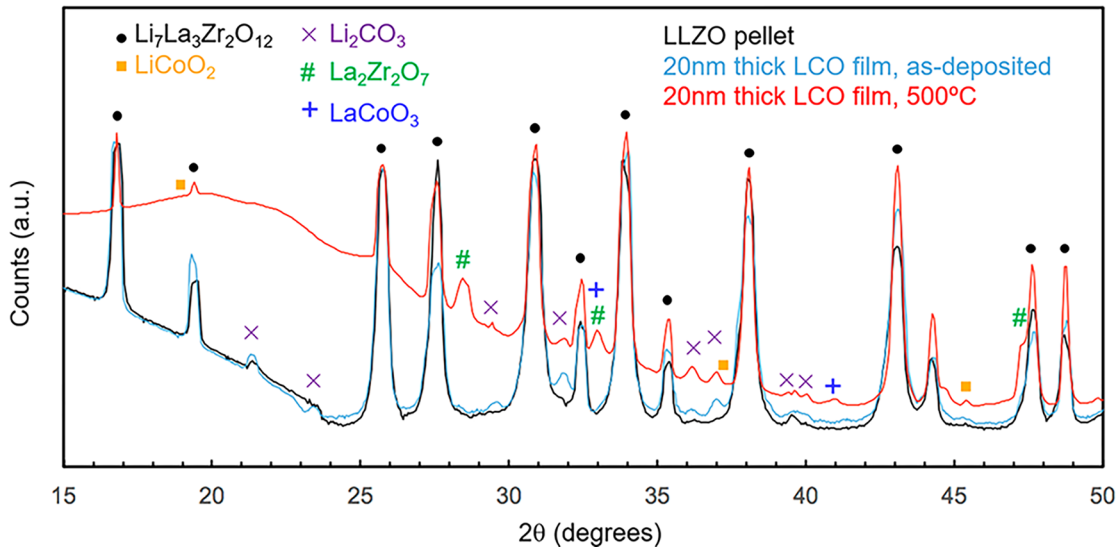

Figure 10. Synchrotron XRD spectra for the LLZO pellet and the 20 nm LCO film on LLZO in the as-deposited state and after annealing at 500 °C.

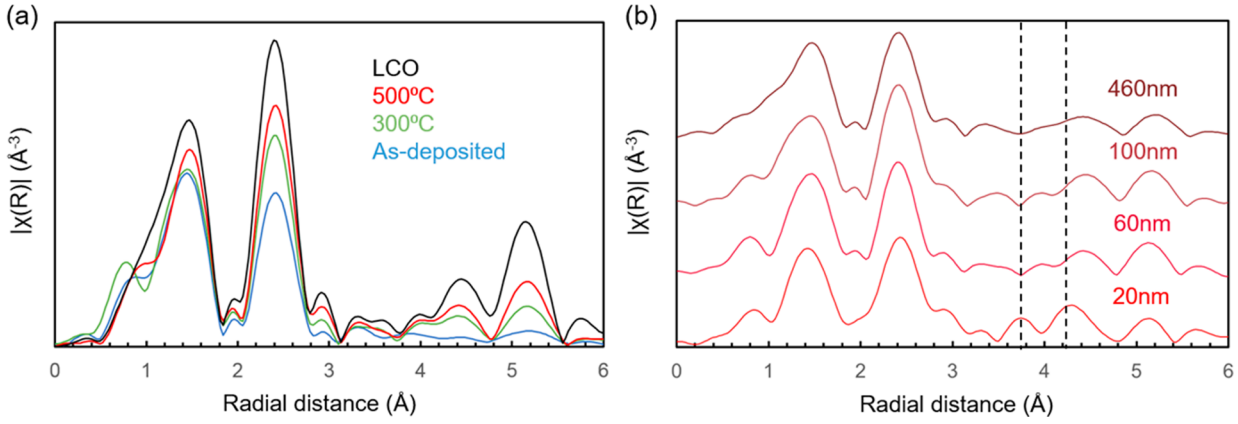

Figure 11. (a) Fourier transform of Co extended X-ray absorption fine structure spectra for LCO powder reference sample, LCO|LLZO samples with a 460 nm deposited LCO layer, in the as-deposited state, and after annealing at 300 and 500 °C. (b) Fourier transform of Co extended X-ray absorption fine structure spectra for LCO|LLZO samples with 20, 60, 100, and 460 nm deposited LCO layers after annealing at 500 °C.

D. Secondary Phase Formation at the LCO|LLZO Interfaces. The structure of the phases as a result of the reaction between the LCO film and the LLZO pellet was examined by synchrotron XRD and EXAFS. While XRD is sensitive to crystalline states, XAS can be used to detect the onset of reactions even if they have not yet formed a phase with long-range crystalline order. Figure 10 shows XRD spectra collected from the LLZO pellet and 20 nm LCO films on LLZO in the as-deposited state and after annealing at 500 °C. The XRD spectrum for the LLZO pellet showed reflections for both cubic LLZO and Li_2CO_3 (ICDD: 96-900-8284). For the as-deposited LCO|LLZO sample, a small peak from LCO was observed at 2θ = 45.3° in addition to those from LLZO and Li_2CO_3. Intensities from the Li_2CO_3 were more prominent for the LCO|LLZO sample. A 500 °C anneal of that sample induced the appearance of many new XRD peaks. The emergence of $La_2Zr_2O_7$ (ICDD: 04-015-3304) could be observed clearly, and the broad peak at lower angles ($\lesssim$25°) suggests the growth of semiamorphous phases. It is also possible that $LaCoO_3$ is a secondary phase that emerges as a result of annealing. However, this was difficult to conclude because many of the $LaCoO_3$ reflections overlap with those of LLZO, except one. The two most intense peaks for $LaCoO_3$ [(110) at 32.98° (100% intensity) and (104) at 33.30° (99.2% intensity)] overlap with the broad $La_2Zr_2O_7$ (400) peak at 33.37°. The second most intense peak for $LaCoO_3$ (024) at 47.57° (55.2% intensity) overlaps with the LLZO(631) peak at 47.41°. The third most intense peak for $LaCoO_3$ (012) at 23.27° (29.0% intensity) is obscured by the broad semi-amorphous peak at the lower angles. This leaves only the fourth most intense peak for $LaCoO_3$ (202) at 40.75° (25.2% intensity) for phase identification. The $LaCoO_3$ (214) peak at 59.10° (30.9% intensity) was not accessible due to the angular limit in the synchrotron XRD setup. Similar peak overlap issues have hindered the identification of secondary phases in cathode|LLZO powder mixtures previously.[63] Similar measurements were conducted with a laboratory XRD system using thicker LCO layers. Again, the emergence of $La_2Zr_2O_7$ peaks was observed after high temperature annealing (Figure S9).

Figure 11(a) shows Fourier transforms (FT) of the k^3-weighted Co K-edge EXAFS oscillations from 460 nm LCO films on LLZO in the as-deposited state and after annealing at 300 and 500 °C. The FT plots highlight the radial distances associated with the scattering events. The first-shell Co−O and

DOI: 10.1021/acs.chemmater.8b01713
Chem. Mater. 2018, 30, 6259−6276

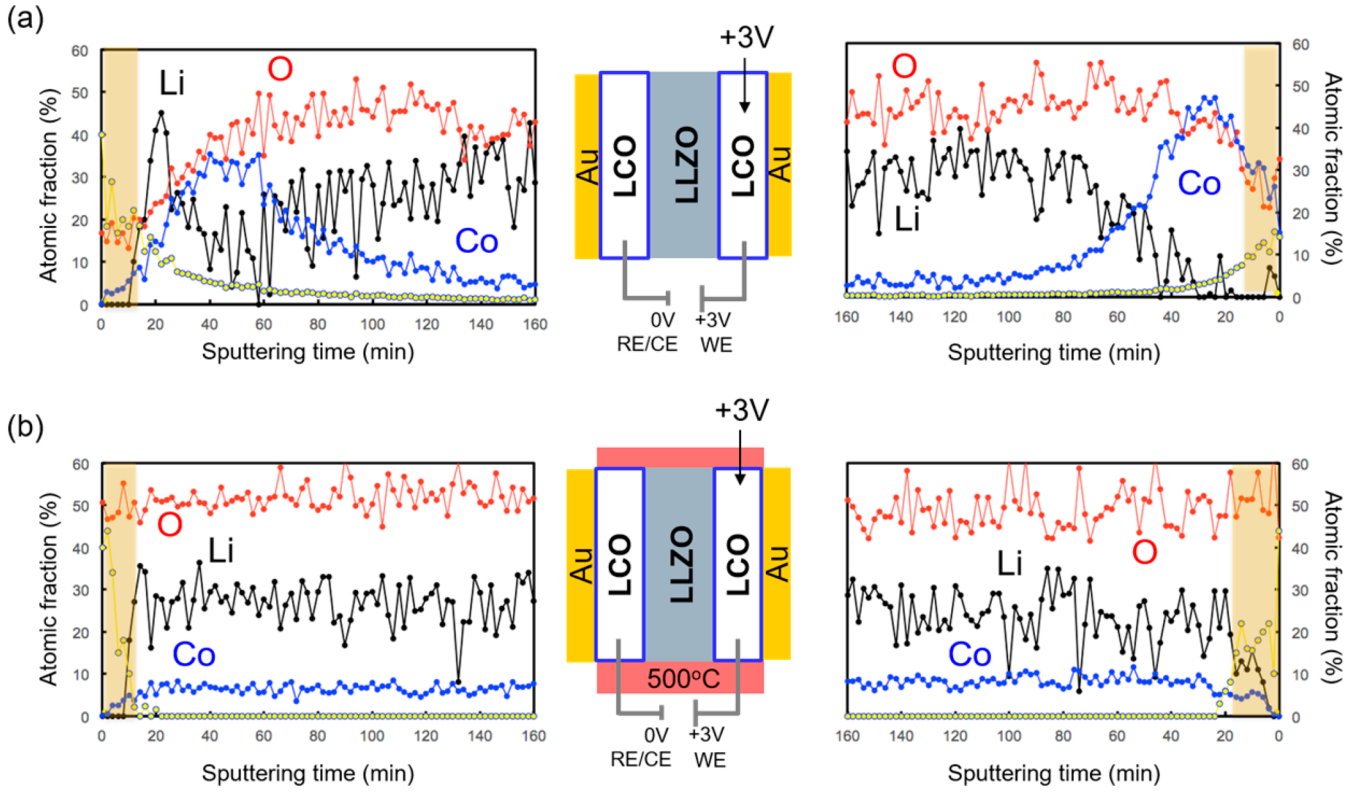

Figure 12. Li, Co, O, and Au depth profiles through the Au electrodes (marked in yellow) using X-ray photoelectron spectroscopy taken on both sides of two symmetric LCO|LLZO|LCO cells with 60 nm deposited LCO layers on LLZO after a potentiostatic hold at 3 V for 1 h. (a) Data taken on an as-prepared cell and (b) data taken on a cell after it was annealed at 500 °C for 4 h.

Co−Co scattering events were represented strongly at 1.4 and 2.4 Å. The coordination associated with first-shell Co−O and Co−Co scattering events increased as a result of annealing. While it is known that RF sputtering at room temperature produces low-crystallinity films,[70] depositing the LCO films at room temperature and then annealing the LCO|LLZO structures at certain temperatures was necessary to control cation diffusion at the interface. The trend in the Co fine structure as a function of temperature indicates that the LCO films improve their crystallinity with annealing. This result also agrees with TEM and *ex situ* XAS findings that suggest a larger fraction of crystalline LCO after annealing.

The Co EXAFS references indicate that there is no evidence of Co_3O_4 impurities in the LCO films. (The reference Co_3O_4 EXAFS data is presented in Figure S10.) After annealing at 500 °C, the EXAFS results for the LCO film agree well with the LCO powder reference sample. The results of fitting the LCO EXAFS spectra with individual scattering paths are presented in Figure S11 and Table S1.

Figure 11(b) shows Fourier transforms of the k^3-weighted Co K-edge EXAFS oscillations for LCO|LLZO samples with different LCO layer thicknesses after annealing at 500 °C. The EXAFS spectra for 460, 100, and 60 nm films agree well with the LCO reference sample in terms of the radial positions of the peaks. However, for the 20 nm sample, EXAFS peaks in the range of 3.8 and 4.3 Å are observed. Reference spectra for $La_{0.6}(Sr_{0.4})CoO_3$ show prominent EXAFS features between 3 and 4.3 Å[71−73] (see Figure S10). The EXAFS spectra for the 20nn sample was fit using calculated $LaCoO_3$ paths (simulated using FEFF9.0[74,75]), and it was determined that these scattering peaks could correspond to Co−La−O scattering events (see Figure S12 and Table S2). Therefore, it is possible that the 20 nm LCO film after annealing at 500 °C has characteristics of a La−Co−O phase near the LCO|LLZO interface.

EXAFS spectra were collected for Zr and La in fluorescence mode for various LCO thickness films and under different annealing conditions. However, Zr and La are present in the bulk of the LLZO pellet as well as at the interface, and the signal depth in this measurement mode is large. Therefore, it was not possible with these results to deduce any changes associated with La and Zr coordination at the LCO|LLZO interface compared to bulk LLZO (see Figure S13).

E. Electrochemical Degradation of the LCO|LLZO Interfaces. To assess modifications to the interface resistance due to the chemical and structural changes presented above, two types of experiments were performed: one profiled the Li distribution after a potentiostatic hold and the other quantified the interface impedance with both experiments performed on symmetric cells. Figure 12 shows the Li, Co, O, and Au profiles obtained by XPS for two symmetric LCO|LLZO|LCO cells after a 3 V potentiostatic hold using Li-ion blocking Au electrodes. One measurement was conducted in the as-deposited state with the other after annealing at 500 °C. The current responses during the 3 V potentiostatic hold are plotted in Figure S15. For the as-deposited LCO|LLZO|LCO cell, the potentiostatic hold was able to move Li through the LCO|LLZO interfaces. One LCO electrode was polarized at 3 V. As a result, the opposite LCO electrode was depleted in Li (Figure 12(a), right). As expected, the LCO electrode that was held at 3 V did not intercalate more Li but rather plated out Li between LCO and Au contact (Figure 12(a), left). It is clear that the Li peak does not overlap with the Co profile peak, and the Li profile within the LCO region (where Co peaks) is

DOI: 10.1021/acs.chemmater.8b01713
Chem. Mater. 2018, 30, 6259−6276

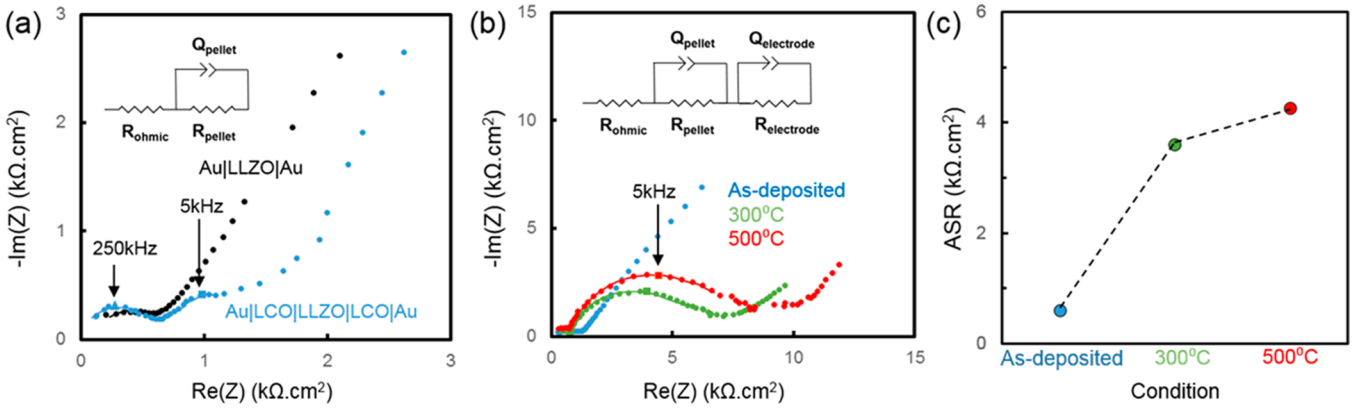

Figure 13. (a) Electrochemical impedance spectroscopy data acquired at room temperature for Au|LLZO|Au and Au|LCO|LLZO|LCO|Au symmetric cells in the as-deposited state. (b) Electrochemical impedance spectroscopy data for Au|LCO|LLZO|LCO|Au symmetric cells in the as-deposited state and after annealing at 300 and 500 °C. (c) ASR values for the LCO|LLZO interface in the as-deposited state and after annealing at 300 and 500 °C.

consistent with the unpolarized profile shown in Figure 2(a). The Li profile peak in this potentiostatically held electrode is rather between Au and LCO. The shape of the Li 1s peak taken at the position where the Li concentration profile peaks also confirms the formation of metallic lithium (Figure S16).[76] The Co 2p spectrum taken from the left side of the cell upon potentiostatic hold also shows LCO layer still has Co-oxide binding environment and not Co metal (see Supporting Information file for explanation of this process in the symmetric cell). As a result, in this experiment, we could flow Li from the right to the left side of the symmetric cell and formed *in situ* a cell configuration that represents nearly a full cell, as Au|Li|LCO|LLZO|LCO(delithiated)|Au with delithiation of one LCO electrode and Li plating on the opposite electrode.

For the LCO|LLZO|LCO cell that was annealed at 500 °C, the same potentiostatic hold experiment yielded no difference in the Li profiles on either side of the symmetric LCO|LLZO|LCO cell. The absence of a change in Li content from the right to the left LCO electrode in Figure 12(b) demonstrates that Li transport was blocked at the LCO|LLZO interfaces and it does not flow after annealing the cell at 500 °C. This is also consistent with the largely smeared Co profile, as also shown in Figure 2. As a result, we can conclude that the thermal effect on interface chemistry dominates over the presence of even a large potential at this interface.

Figure 13(a) shows EIS spectra for an LLZO pellet and a symmetric LCO|LLZO|LCO sample with 60 nm as-deposited LCO layers using Li-ion blocking Au electrodes. Over the studied frequency range, a semicircle and a low-frequency tail can be observed for the LLZO pellet. The low-frequency tail is due to the blocking nature of the Au electrodes.[77−79] The semicircle is characterized by a frequency of 250 kHz and is present in all measurements with LLZO pellets. The EIS spectra for the LLZO pellet was simulated using an $(R_{ohmic})(R_{pellet}Q_{pellet})$ equivalent circuit model, where the R_{ohmic} element accounts for the resistance associated with measurement setup and the $(R_{pellet}Q_{pellet})$ element accounts for the bulk conduction in the LLZO pellet. The value for R_{ohmic} is less than 20 Ω.cm^2 for all cells measured. Fitting the LLZO pellet EIS spectra with a $(R_{ohmic})(R_{pellet}Q_{pellet})$ circuit reveals that the 250 kHz semicircle has an equivalent capacitance value of ∼10^{-9} F. The bulk and grain boundary transport capacitances in LLZO are expected to be on the order of 10^{-12} F and 10^{-9} F, respectively.[80] Therefore, the semicircle characterized by 250 kHz is assigned to be the impedance associated with grain boundary conduction. The intergrain and grain boundary contributions to bulk LLZO conduction could not be distinguished at room temperature, which is the case for many reports on LLZO in the literature.[41,77] The Li-ion conductivity of the LLZO pellet, calculated using R_{pellet} and the dimensions of the sample, is 0.19 mS/cm, in agreement with cubic LLZO conductivities reported in literature.[14]

The symmetric LCO|LLZO|LCO sample exhibits an additional semicircle with a peak at 5 kHz, which can be assigned to the LCO|LLZO interface because this semicircle is not present for the LLZO pellet (Figure 13(a)). Figure 13(b) shows EIS data for the symmetric LCO|LLZO|LCO samples in the as-deposited state and after annealing at 300 and 500 °C. The EIS data were fitted with the model used for the LLZO pellet and an additional $(R_{electrode}Q_{electrode})$ element to account for the LCO|LLZO interface.[51] The capacitance value associated with the $(R_{electrode}Q_{electrode})$ element is ∼10^{-7} F, which is consistent with other values reported for electrode interactions.[80] The $R_{electrode}$ element corresponds to an area specific resistance (ASR) associated with the LCO|LLZO interface. Because the $R_{electrode}$ element includes contributions from two identical LCO|LLZO interfaces, the value of $R_{electrode}$ was divided by two to obtain the ASR of a single LCO|LLZO interface.[39] Figure 13(c) shows that the ASR associated with LCO|LLZO interfaces increases significantly after annealing at 300 and 500 °C, compared to the as-deposited state. The value of the LCO|LLZO ASR increases from 0.6 kΩ.cm^2 in the as-deposited state to 3.6 and 4.3 kΩ·cm^2 after annealing at 300 and 500 °C, respectively. These ASR values for the LCO|LLZO interfaces found here are on the same order as previously reported ASR values for LCO|LLZO interface created by high-temperature pulsed laser deposition.[51,81] The relative increase in ASR upon annealing here is consistent with the decrease of the initial current during the potentiostatic-hold, down to ∼23% of the as-prepared LCO|LLZO|LCO structure upon annealing at 500 °C (see Figure S15).

■ DISCUSSION

As seen from a comprehensive set of experimental results reported above, there is evidence for significant cation intermixing and a solid phase reaction at the LCO|LLZO

DOI: 10.1021/acs.chemmater.8b01713
Chem. Mater. 2018, 30, 6259−6276

interface as a result of annealing in air. Specifically, Co and La are observed to intermix at the interface based on results from STEM EDX, XPS, SIMS, and HAXPES. The significant redistribution of Co indicates that the LCO phase decomposes near the interface. As a consequence, excess Li is available for reaction with CO_2 to form Li_2CO_3 throughout the surface, the LCO layer, and the near-interface zone, as shown in Figure 2. The out-diffusion of La is consistent with decomposition of LLZO into relatively La-poor phases such as $La_2Zr_2O_7$, as also confirmed by XRD. The cross-diffusion of La and Co, and EXAFS and XRD signatures, strongly suggest the emergence of a La−Co−O phase. Previous studies of LCO|LLZO interface reactions indicated the formation of La−Co−O phases such as La_2CoO_4 and $LaCoO_3$.[49,50,63] Zr shows negligible, if any, reactivity with LCO for the annealing conditions studied in this report. The decomposition reaction creates excess La available for out-diffusion, leaving behind Zr stably in the reaction product $La_2Zr_2O_7$. It is possible that the resulting picture from this observation is that the $La_2Zr_2O_7$ forms closer to the LLZO interface, and the La−Co−O phases form closer to the top surface.

O K-edge measurements can be used to clearly distinguish between the LCO, LLZO and Li_2CO_3 phases.[39] These measurements were performed in the fluorescence (*ex situ*) and electron (*in situ*) yield mode to probe the reaction at the LCO|LLZO interface as a function of temperature. In these measurements, the peak associated with LLZO (532 eV) decreased in comparison to the LCO (530 eV) and Li_2CO_3 (534 eV) peaks. This indicated that LLZO near the interface decomposes with increasing annealing temperature. This is consistent with the eventual formation of $La_2Zr_2O_7$, as identified by XRD. The O K-edge peaks for $La_2Zr_2O_7$ are at 531 and 533.8 eV.[82] Another possible decomposition product, $LaCoO_3$, exhibits O K-edge peaks at 530 and 535 eV.[83] Yet another possible decomposition product, La_2CoO_4, exhibits O K-edge peaks at 529.5 and 532 eV.[84] Therefore, the decomposition of LLZO into either $La_2Zr_2O_7$ or $LaCoO_3$ would result in a decrease of the XAS intensity at 532 eV. Because O K-edge peak for La_2CoO_4 is at 532 eV, this could point that $LaCoO_3$ is the more likely La−Co−O decomposition phase rather than La_2CoO_4. The preference to $LaCoO_3$ is also supported by the observation of the $LaCoO_3$ (202) XRD peak at 40.75° in the LCO|LLZO sample after annealing at 500 °C. It was not possible to identify $La_2Zr_2O_7$ or $LaCoO_3$ clearly in the O K-edge XAS because their peaks overlap with those of LCO and Li_2CO_3.

It is worth it here to compare our experimental finding to the previously reported computational and experimental studies.[50,58−60,63] $La_2Zr_2O_7$ as a result of reactions between LCO and LLZO was proposed by those earlier works, which was also found by the XRD and XAS in this study. Formation of a La−Co−O phase was not predicted computationally but has been suggested in several experimental papers.[49,50,63] In this work, we conclude that $LaCoO_3$ is the more likely La−Co−O phase, rather than La_2CoO_4, due to the O K-edge XAS data and XRD. Several computational studies predicted the formation of La_2O_3 as a decomposition product of LLZO.[58−60] In this work, there is no evidence from XRD or EXAFS analysis for the formation of La_2O_3. In computational studies, several Li-rich Li−Co−O phases (Li_2CoO_3[58], Li_5CoO_4,[60] and $Li_7Co_5O_{12}$[60]) were predicted as a result of LCO decomposition. In this study, we did not observe any evidence (by composition or by structural analysis) to the formation Li-rich LCO phases. This is likely because the previous computational studies did not consider Li_2CO_3 as a decomposition product in the presence of CO_2 in the environment, as a means to uptake Li instead of Li-rich LCO phases.

The secondary phases that were detected in this study (Li_2CO_3, $La_2Zr_2O_7$, and $LaCoO_3/La_2CoO_4$) are known to be poor Li conductors.[14,39,85] Therefore, it is not surprising that annealing LCO|LLZO samples is detrimental to the battery performance. Depth profiles of Li measured across LCO|LLZO|LCO symmetric cells upon a potentiostatic hold unequivocally demonstrate that Li transfer is blocked across these interfaces as a result of annealing. Consistent with that observation, the ASR of the interface increased up to 8 times that of the as-prepared (not annealed) sample, according to EIS measurements. In addition to the secondary phases that form at the interface, there is a morphological change at the interface between LCO|LLZO and possible void formation, as shown in the TEM studies, which could also result in an increase in the ASR of the interface.

It is possible that the presence of an electrochemical potential at the LCO|LLZO interface could also induce a decomposition reaction at the interface. However, the magnitude of the decomposition as a result of potentiostatic hold at 3 V in this symmetric cell experiment was negligible compared to the reaction induced by annealing at 500 °C for 4 h. The compositional profile of the nonpolarized (Figure 2(a)) and polarized LCO|LLZO interfaces (Figure 12(a)) show similar La, Zr and Co profiles. The cation profiles for LCO|LLZO interface after annealing at 500 °C also look similar for the nonpolarized (Figure 2(c)) and polarized cases (Figure 12(b)). Therefore, the dominant decomposition effect appears to be the thermal effect rather than the polarization effect in the instability of the LCO|LLZO interface.

The reaction zone between the LCO and LLZO is expected to be temperature-dependent. Choosing the optimal annealing parameters to bond a ceramic cathode and LLZO in a solid-state battery will depend on knowledge of the reaction width and chemistry as a function of temperature. XRD is an extremely useful technique in identifying emerging phases. However, it is a bulk-sensitive measurement with limited utility for interface studies, unless performed in a special geometry. Previous research reported mixing different ratios of cathode and LLZO powders and annealing them at relatively high temperatures (above 500 °C) before the observation of new peaks in the XRD scans.[47,56,63] This is because higher temperatures are necessary for the crystallinity and volume fraction of secondary phases to reach XRD-detection levels. In our work, the thin film configuration of the samples and the spectroscopic measurements that do not require long-range crystallinity allows us to deduce the onset of interface reactions at relatively low temperatures, below 500 °C. By depositing LCO layers at room temperature, the formation of a reaction layer in our samples prior to annealing was avoided or minimized. By changing the thickness of the LCO films on LLZO, it is possible to identify the reaction zone width as a function of temperature. HAXPES measurements on the 5, 20, 60, and 100 nm LCO films show that annealing them at 500 °C for 4 h results in a ∼100 nm-thick reaction zone at the LCO|LLZO interface. At 250 °C, the reaction zone was less than 20 nm. In summary, the onset of degradation at the LCO|LLZO interface starts to take place at temperatures (300−500 °C) much lower than those in typical ceramic sintering and bonding. The temperatures that have been reported for LCO

DOI: 10.1021/acs.chemmater.8b01713
Chem. Mater. 2018, 30, 6259−6276

deposition and cosintering in the literature are all above 500 °C. At this temperature, we found significant reaction and degradation affecting a thickness near the interface over >100 nm. This finding was only possible by using interface-sensitive measurement techniques and well-defined thin films. Going forward, other densification methods such as very fast spark plasma sintering,[86−88] or humidity-assisted room-temperature sintering[89] might be desirable to bond ceramic cathodes to LLZO without the formation of extensive reaction zones.

Although garnet solid-state electrolytes such as LLZO are considered more stable in air than sulfide solid-state electrolytes, their surfaces are still susceptible to Li_2CO_3 formation.[27] Similarly, LCO reacts with CO_2 to form Li_2CO_3 on its surface.[90] The Li_2CO_3 thickness on LCO increases with annealing in an atmosphere containing CO_2, as XPS depth profiling shows. The effect of Li_2CO_3 on Li|LLZO interfaces has been studied thoroughly by symmetric cell cycling and spectroscopy.[27] In this work, we show that Li_2CO_3 forms also at the LLZO|LCO interface, and within the LCO near this interface, and is detrimental for the interface impedance. Moreover, it is possible to remove Li_2CO_3 from the LLZO and LCO surfaces by heating the samples in a pure O_2 atmosphere. The Li_2CO_3 layer was removed from LCO and LLZO at 250 °C and 350 °C respectively, in 30 mTorr of O_2. Polishing the surface of LLZO in a carbon-free environment has been proposed as an effective means of avoiding Li_2CO_3 formation prior to anode or cathode deposition. Annealing the LLZO under O_2 or other carbon-free gases could be an alternative method for Li_2CO_3 removal.[37]

CONCLUSIONS

The interface between Li cathode materials and LLZO is of significant interest to the solid-state battery development. Several studies have focused on identifying the secondary phases and compositional profiles across the interface. The present work focuses on systematically studying the effect of annealing temperature on the LCO|LLZO interface using thickness-controlled thin films and interface-sensitive detection methods. XPS, SIMS, HAXPES, and STEM EDX results show that Co and La diffuse extensively across the LCO|LLZO interface. As a result of annealing in air up to 500 °C, the most likely reaction products at this interface are Li_2CO_3, $La_2Zr_2O_7$, and $LaCoO_3$, as identified by XRD, XAS, and EXAFS. The interface reaction width was found in HAXPES and *in situ* XPS measurements to be less than 20 nm at 250 °C and close to 100 nm at 500 °C. These reaction products at the LCO|LLZO interface are detrimental. Depth profiling of Li across the interfaces shows that the reacted interfaces block Li transfer, leading to an eightfold increase in the interface impedance. The exposure of LCO and LLZO to the atmosphere induces Li_2CO_3 formation; however, the Li_2CO_3 on the surface could be completely removed by heating the sample to 350 °C under an O_2 atmosphere. The thin-film cathode geometry and the interface-sensitive measurement techniques allow us to observe the formation of interface reaction products at temperatures much lower than in traditional ceramic sintering and bonding processes. Our results indicate that processing conditions at lower temperatures, short time scales, and in CO_2-free environments are highly desirable for obtaining ceramic cathode−electrolyte interfaces that enable fast Li transfer and high capacity.

EXPERIMENTAL PROCEDURES

Sample Preparation. Cubic LLZO powders (dopant: Al, 99.9%) were purchased from MSE Supplies (Arizona, United States). Phase purity of LLZO powders were confirmed by XRD. LLZO powder were pressed into pellets (10 mm diameter, 1 mm thickness) and sintered at 1150 °C for 8 h in air. Sacrificial LLZO pellets were placed under and above the LLZO pellet of interest during sintering to minimize Li loss. The LLZO pellets were polished with 800, 1200, and 2400-grit SiC paper to a mirror finish. Immediately prior to LCO deposition, LLZO surfaces were dry-polished with 2400-grit SiC paper to remove surface Li_2CO_3 layer.

LCO layers were deposited by radio frequency (RF) sputtering in an argon−oxygen atmosphere from an LCO target. The argon to oxygen ratio during sputtering was 3:1 (9 Ar sccm: 3 O_2 sccm). The LCO films were deposited on LLZO pellets at room temperature. The sputtering deposition rate of the LCO layer was determined using a quartz balance in the sputtering chamber. Postannealing steps were 300 and 500 °C for 4 h in an air atmosphere.

Transmission Electron Microscopy (TEM). Specimens for TEM analysis were prepared by conventional lift-out procedure using a dual-beam SEM equipped with a Ga^+ focused ion beam column (Helios Nanolab 600, Thermo Fisher Scientific). Specimen thinning to a final thickness of ∼50 nm was performed using ion beam accelerating voltages ranging from 30−2 kV, and specimen tilt of ±3° relative to the optic axis of the ion beam. TEM specimens were stored in an Ar glovebox, though reaction with the atmosphere during sample handling is expected to form surface phases on the TEM specimen surfaces, which may have resulted in amorphous contrast visible in HRTEM images. TEM and STEM analyses were performed using a JEOL 2010F operating at 200 kV; for EDX, the STEM probe diameter was ∼1 nm. The profiles presented in Figure 1 are a qualitative indication of elemental distribution with the intensity in each cation's profile defined by normalizing its detected X-ray counts by the sum of all ion counts, e.g. eq 1 exemplified for Co. This normalization also effectively accounts for variation in specimen thickness.

$$I_{Co} = \frac{I_{Co}}{I_{Co} + I_{Zr} + I_{La} + I_{O}} \quad (1)$$

Elemental profiles were fit using the logistic function

$$f(x) = \frac{s}{1 + e^{-k(x-x_0)}} + y \quad (2)$$

where s scales the fit vertically, k defines the steepness of the sloped transition region spanning the interface, x is the position along the line scan, x_0 is the x position where the value of the fit is 50% of the difference between maximum and minimum fit values, and y shifts the fit vertically. Least-squared fitting was implemented in Python. The calculated chemical widths are so-called 10−90% widths, defined by the separation of x positions corresponding to 10 and 90% of the maximum fit values after scaling the fit between zero and one.

X-ray Photoelectron Spectroscopy and X-ray Absorption Spectroscopy. XPS profiling measurements were carried out with a Kratos Axis Ultra spectrometer using a monochromatic Al Kα source. The sputtering of the sample was performed with an Ar ion source (2 μA) over a 2 mm by 2 mm area. The sample was rotated during the sputtering to ensure homogeneous removal of material from the surface. Detailed scans for Li 1s, Co 2p, O 1s, La 3d, Zr 3d, and C 1s were collected after every 2 min of Ar sputtering. The quantification of the atomic concentrations were performed using the Multipak software and the relative sensitivity factors in the Multipak software. The Co/Li ratios were calculated by dividing the atomic percentage of Co with Li.

Ex situ Co L-edge and O K-edge XAS spectra were measured at the CSX-2 (23-ID-2) beamline at the National Synchrotron Light Source II. Partial fluorescence yield (PFY) spectra were collected using a Vortex silicon drift detector. Samples were preannealed prior to loading into the UHV chamber, and measurements were done at room temperature.

DOI: 10.1021/acs.chemmater.8b01713
Chem. Mater. 2018, 30, 6259−6276

In situ heating XPS and XAS measurements were carried out at the 9.3.2 beamline at Advanced Light Source (ALS) in PFY mode.[91] The sample was heated from a heater in the back of the sample holder, and the temperature was measured using a thermocouple on the surface of the sample. The atmosphere in the chamber during the heating experiment was 30 mTorr of pure O_2. XPS measurements were taken at a photon energy of 760 eV. XAS scan of the O K-edge were taken over 515−560 eV with a detection energy of 210 eV.

Hard X-ray photoelectron spectroscopy measurements were carried out at 33-ID beamline at Advanced Photon Source (APS) with a photon energy of 10 keV. The angle between the detector and sample surface was changed from 60° to 85° to change the detection depth. The elemental ratios were calculated after fitting the spectra with CasaXPS software. The photoionization cross sections decay significantly at higher photon energies. The XPS peaks used for elemental ratio analysis (Co 3d with Li 1s and La 3d with O 1s) show similar cross section decay with respect to photon energy up to 1.5 keV (see Figure S14). If the decay in cross section is assumed to be linear up to 10 keV, then the elemental ratios could be calculated using the sensitivity factors for Al Kα source X-rays. Furthermore, the La/O ratio (~0.25) calculated from the reference LLZO sample using hard (10 keV) X-ray photoelectron spectroscopy experiments matches closely with soft (1.5 eV) X-ray photoelectron spectroscopy measurements, and therefore, the assumption that the ratio of photoionization cross sections for La 3d and O 1s is similar at 1.5 eV and 10 keV is assumed valid.

EXAFS measurements were carried out at 10-ID MRCAT-(Materials Research Collaborative Access team) beamline at APS for Co K-edge (7709 eV), La L_3-edge (5483 eV) and Zr K-edge (17998 eV). Data alignment, summation, calibration, and error correction was done with Athena software.[92] Spectral fitting of the LCO powder spectra was done with Artemis software using theoretical EXAFS paths created with FEFF6.0. The reference spectra for compounds were calculated using the FEFF9.0 software and CIF files obtained from the International Crystal Database.

Secondary Ion Mass Spectroscopy. SIMS measurements were performed using a focused ion beam (FIB)-SIMS instrument. The current of gallium ion flux was 593pA. The samples are required to be tilted at 30° toward the HIDEN SIMS detector during the FIB-SIMS depth profile analyses for optimum secondary ion detection. The area selected for FIB-SIMS depth profiles are 20 μm^2 areas with the sample tilted so that the actual area on the sample is rectangular with the crater side in the direction of the tilt being slightly longer at ~23.1 μm.

Both polarity SIMS ions are detected simultaneously during the depth profiles. The FEI SIMS detector is set up for negative ion detection and HIDEN SIMS detector set up for positive ion detection. Typical positive and negative SIMS mass spectra were obtained before depth profiling to check on the correct peak positions on the mass/charge scale of the secondary ions of interest for each detector used during the depth profiles. Both polarity SIMS ions are detected simultaneously during the depth profiles.[93] The FEI SIMS detector is set up for negative ion detection and HIDEN SIMS detector set up for positive ion detection. Typical positive and negative SIMS mass spectra were obtained before depth profiling to check on the correct peak positions on the mass/charge scale of the secondary ions of interest for each detector used during the depth profiles.

X-ray Diffraction. XRD measurements on 20 nm LCO deposited samples were carried out at 33-ID beamline at APS with a photon energy of 10 keV. The 2θ angles from the 10 keV measurements were converted to 2θ values for a Cu Kα source to simplify phase identification. The XRD measurements on 460 nm LCO deposited samples were performed with a PANalytical X'Pert Pro with a Cu Kα source.

Electrochemical Impedance Spectroscopy (EIS). EIS measurements were performed with a PARSTAT400 potentiometer in the 5 MHz to 1 Hz range with a potential amplitude of 100 mV. The Au electrodes were coated using RF sputtering and had an approximate thickness of 100 nm. The edges of the Au-coated sintered pellets were polished to avoid a short circuit. Au electrodes were deposited after the annealing step for the LCO|LLZO|LCO cells to avoid diffusion of Au with LCO layers. EIS spectra were fit with equivalent circuit models using EC-Lab software.

■ ASSOCIATED CONTENT

Supporting Information

The Supporting Information is available free of charge on the ACS Publications website at DOI: 10.1021/acs.chemmater.8b01713.

SEM, XRD, and XRR information on deposited LCO layers. Cross-sectional STEM EDX analysis of the LCO|LLZO interface. Configuration of the HAXPES data collection setup. Carbonate to carbon ratio as determined by HAXPES measurements. Zr K-edge and La L_3-edge EXAFS data. O K-edge XAS measurements. O 1s, Li 1s, Zr 3d, and La 4d in situ XPS measurements. XRD data for LCO|LLZO samples. Fourier transforms of Co K-edge EXAFS data for reference samples. EXAFS Fourier fitting for LCO reference sample and 20 nm LCO|LLZO interface. Fourier transforms of Zr K-edge and La L_3-edge EXAFS data. Photoionization cross sections for La 3d, O 1s, Co 3d, and Li 1s. Current vs time data for potentiostatic hold experiment. Li 1s, Co 3d, and Co 2p XPS data during the XPS profiling experiment (PDF)

■ AUTHOR INFORMATION

Corresponding Author

*E-mail: byildiz@mit.edu.

ORCID

Gulin Vardar: 0000-0001-5458-9568
Qiyang Lu: 0000-0002-9155-3684
Ainara Aguadero: 0000-0001-7098-1033
Adrian Hunt: 0000-0002-5283-9647
Iradwikanari Waluyo: 0000-0002-4046-9722
Ethan J. Crumlin: 0000-0003-3132-190X
Yet-Ming Chiang: 0000-0002-0833-7674
Bilge Yildiz: 0000-0002-2688-5666

Present Address

△G.V.: Department of Mechanical Engineering, Bogazici University, Istanbul 34342, Turkey.

Notes

The authors declare no competing financial interest.

■ ACKNOWLEDGMENTS

The authors acknowledge the support of the Bosch Energy Research Network (BERN) grant, the MIT Energy Initiative, and MISTI MIT-Imperial College grant. This work made use of the MRSEC Shared Experimental Facilities at MIT, supported by the National Science Foundation under Award DMR 14-19807. D.D.F. was supported by the U.S. Department of Energy, Office of Science, Materials Sciences and Engineering Division. Use of the Advanced Photon Source was supported by the U.S. Department of Energy, Office of Science, Office of Basic Energy Sciences, under Contract No. DE-AC02-06CH11357. MRCAT operations are supported by the Department of Energy and the MRCAT member institutions. This research used resources of the 23-ID-2 beamline of the National Synchrotron Light Source II, a U.S. Department of Energy (DOE) Office of Science User Facility

DOI: 10.1021/acs.chemmater.8b01713
Chem. Mater. 2018, 30, 6259−6276

operated for the DOE Office of Science by Brookhaven National Laboratory under Contract No. DE-SC0012704. The Advanced Light Source is supported by the Director, Office of Science, Office of Basic Energy Sciences, of the U.S. Department of Energy under Contract No. DE-AC02-05CH11231. The authors thank Zhan Zhang, Jon Tischler, Joshua Wright, John Katsoudas, Fatih Piskin, and Maximilian Jensen for their help with experiments at beamlines.

REFERENCES

(1) Janek, J.; Zeier, W. G. A Solid Future for Battery Development. *Nat. Energy* **2016**, *1*, 16141.
(2) Luntz, A. Beyond Lithium Ion Batteries. *J. Phys. Chem. Lett.* **2015**, *6*, 300−301.
(3) Goodenough, J. B.; Kim, Y. Challenges for Rechargeable Li Batteries. *Chem. Mater.* **2010**, *22*, 587−603.
(4) Tarascon, J. M.; Armand, M. Issues and Challenges Facing Rechargeable Lithium Batteries. *Nature* **2001**, *414*, 359−367.
(5) Kim, J. G.; Son, B.; Mukherjee, S.; Schuppert, N.; Bates, A.; Kwon, O.; Choi, M. J.; Chung, H. Y.; Park, S. A Review of Lithium and Non-Lithium Based Solid State Batteries. *J. Power Sources* **2015**, *282*, 299−322.
(6) Kim, H.; Jeong, G.; Kim, Y.-U.; Kim, J.-H.; Park, C.-M.; Sohn, H.-J. Metallic Anodes for next Generation Secondary Batteries. *Chem. Soc. Rev.* **2013**, *42*, 9011−9034.
(7) Ong, S. P.; Mo, Y.; Richards, W. D.; Miara, L.; Lee, H. S.; Ceder, G. Phase Stability, Electrochemical Stability and Ionic Conductivity of the Li 10 ± 1 MP 2 × 12 (M = Ge, Si, Sn, Al or P, and X = O, S or Se) Family of Superionic Conductors. *Energy Environ. Sci.* **2013**, *6*, 148−156.
(8) Kato, Y.; Hori, S.; Saito, T.; Suzuki, K.; Hirayama, M.; Mitsui, A.; Yonemura, M.; Iba, H.; Kanno, R. High-Power All-Solid-State Batteries Using Sulfide Superionic Conductors. Nat. *Energy* **2016**, *1*, 16030.
(9) Thangadurai, V.; Pinzaru, D.; Narayanan, S.; Baral, A. K. Fast Solid-State Li Ion Conducting Garnet-Type Structure Metal Oxides for Energy Storage. *J. Phys. Chem. Lett.* **2015**, *6*, 292−299.
(10) Kamaya, N.; Homma, K.; Yamakawa, Y.; Hirayama, M.; Kanno, R.; Yonemura, M.; Kamiyama, T.; Kato, Y.; Hama, S.; Kawamoto, K.; et al. A Lithium Superionic Conductor. *Nat. Mater.* **2011**, *10*, 682−686.
(11) Wang, Y.; Richards, W. D.; Ong, S. P.; Miara, L. J.; Kim, J. C.; Mo, Y.; Ceder, G. Design Principles for Solid-State Lithium Superionic Conductors. *Nat. Mater.* **2015**, *14*, 1026−1031.
(12) Bachman, J. C.; Muy, S.; Grimaud, A.; Chang, H.-H.; Pour, N.; Lux, S. F.; Paschos, O.; Maglia, F.; Lupart, S.; Lamp, P.; et al. Inorganic Solid-State Electrolytes for Lithium Batteries: Mechanisms and Properties Governing Ion Conduction. *Chem. Rev.* **2016**, *116*, 140−162.
(13) Cao, C.; Li, Z.-B.; Wang, X.-L.; Zhao, X.-B.; Han, W.-Q. Recent Advances in Inorganic Solid Electrolytes for Lithium Batteries. *Front. Energy Res.* **2014**, *2*, 25.
(14) Murugan, R.; Thangadurai, V.; Weppner, W. Fast Lithium Ion Conduction in Garnet-Type Li7La3Zr2O12. *Angew. Chem., Int. Ed.* **2007**, *46*, 7778−7781.
(15) Thangadurai, V.; Narayanan, S.; Pinzaru, D. Garnet-Type Solid-State Fast Li Ion Conductors for Li Batteries: Critical Review. *Chem. Soc. Rev.* **2014**, *43*, 4714−4727.
(16) Ohta, S.; Kobayashi, T.; Asaoka, T. High Lithium Ionic Conductivity in the Garnet-Type Oxide Li7-X La3(Zr2-X, NbX)O12 (X = 0−2). *J. Power Sources* **2011**, *196*, 3342−3345.
(17) Rettenwander, D.; Welzl, A.; Cheng, L.; Fleig, J.; Musso, M.; Suard, E.; Doeff, M. M.; Redhammer, G. J.; Amthauer, G. Synthesis, Crystal Chemistry, and Electrochemical Properties of Li 7−2 X La 3 Zr 2− X Mo X O 12 (X = 0.1−0.4): Stabilization of the Cubic Garnet Polymorph via Substitution of Zr 4+ by Mo 6+. *Inorg. Chem.* **2015**, *54*, 10440−10449.
(18) Wagner, R.; Redhammer, G. J.; Rettenwander, D.; Senyshyn, A.; Schmidt, W.; Wilkening, M.; Amthauer, G. Crystal Structure of Garnet-Related Li-Ion Conductor Li 7−3 X Ga X La 3 Zr 2 O 12 : Fast Li-Ion Conduction Caused by a Different Cubic Modification? *Chem. Mater.* **2016**, *28*, 1861−1871.
(19) Thompson, T.; Sharafi, A.; Johannes, M. D.; Huq, A.; Allen, J. L.; Wolfenstine, J.; Sakamoto, J. A Tale of Two Sites: On Defining the Carrier Concentration in Garnet-Based Ionic Conductors for Advanced Li Batteries. *Adv. Energy Mater.* **2015**, *5*, 1500096.
(20) Thompson, T.; Yu, S.; Williams, L.; Schmidt, R. D.; Garcia-Mendez, R.; Wolfenstine, J.; Allen, J. L.; Kioupakis, E.; Siegel, D. J.; Sakamoto, J. Electrochemical Window of the Li-Ion Solid Electrolyte Li7La3Zr2O12. *ACS Energy Lett.* **2017**, *2*, 462−468.
(21) Ma, C.; Cheng, Y.; Yin, K.; Luo, J.; Sharafi, A.; Sakamoto, J.; Li, J.; More, K. L.; Dudney, N. J.; Chi, M. Interfacial Stability of Li Metal-Solid Electrolyte Elucidated via in Situ Electron Microscopy. *Nano Lett.* **2016**, *16*, 7030−7036.
(22) Ohta, S.; Komagata, S.; Seki, J.; Saeki, T.; Morishita, S.; Asaoka, T. All-Solid-State Lithium Ion Battery Using Garnet-Type Oxide and Li3BO3 Solid Electrolytes Fabricated by Screen-Printing. *J. Power Sources* **2013**, *238*, 53−56.
(23) Quartarone, E.; Mustarelli, P. Electrolytes for Solid-State Lithium Rechargeable Batteries: Recent Advances and Perspectives. *Chem. Soc. Rev.* **2011**, *40*, 2525.
(24) Santhanagopalan, D.; Qian, D.; McGilvray, T.; Wang, Z.; Wang, F.; Camino, F.; Graetz, J.; Dudney, N.; Meng, Y. S. Interface Limited Lithium Transport in Solid-State Batteries. *J. Phys. Chem. Lett.* **2014**, *5*, 298−303.
(25) Hartmann, P.; Leichtweiss, T.; Busche, M. R.; Schneider, M.; Reich, M.; Sann, J.; Adelhelm, P.; Janek, J. Degradation of NASICON-Type Materials in Contact with Lithium Metal: Formation of Mixed Conducting Interphases (MCI) on Solid Electrolytes. *J. Phys. Chem. C* **2013**, *117*, 21064−21074.
(26) Bates, J.; Gruzalski, G.; Dudney, N.; Luck, C.; Yu, X. Rechargeable Thin-Film Lithium Batteries. *Solid State Ionics* **1994**, *70−71*, 619−628.
(27) Cheng, L.; Crumlin, E. J.; Chen, W.; Qiao, R.; Hou, H.; Franz Lux, S.; Zorba, V.; Russo, R.; Kostecki, R.; Liu, Z.; et al. The Origin of High Electrolyte-Electrode Interfacial Resistances in Lithium Cells Containing Garnet Type Solid Electrolytes. *Phys. Chem. Chem. Phys.* **2014**, *16*, 18294−18300.
(28) Luntz, A. C.; Voss, J.; Reuter, K. Interfacial Challenges in Solid-State Li Ion Batteries. *J. Phys. Chem. Lett.* **2015**, *6*, 4599−4604.
(29) Tsai, C.-L.; Roddatis, V.; Chandran, C. V.; Ma, Q.; Uhlenbruck, S.; Bram, M.; Heitjans, P.; Guillon, O. Li 7 La 3 Zr 2 O 12 Interface Modification for Li Dendrite Prevention. *ACS Appl. Mater. Interfaces* **2016**, *8*, 10617−10626.
(30) Luo, W.; Gong, Y.; Zhu, Y.; Fu, K. K.; Dai, J.; Lacey, S. D.; Wang, C.; Liu, B.; Han, X.; Mo, Y.; et al. Transition from Superlithiophobicity to Superlithiophilicity of Garnet Solid-State Electrolyte. *J. Am. Chem. Soc.* **2016**, *138*, 12258−12262.
(31) Wang, C.; Gong, Y.; Liu, B.; Fu, K.; Yao, Y.; Hitz, E.; Li, Y.; Dai, J.; Xu, S.; Luo, W.; et al. Conformal, Nanoscale ZnO Surface Modification of Garnet-Based Solid-State Electrolyte for Lithium Metal Anodes. *Nano Lett.* **2017**, *17*, 565−571.
(32) Sharafi, A.; Meyer, H. M.; Nanda, J.; Wolfenstine, J.; Sakamoto, J. Characterizing the Li−Li 7 La 3 Zr 2 O 12 Interface Stability and Kinetics as a Function of Temperature and Current Density. *J. Power Sources* **2016**, *302*, 135−139.
(33) Fu, K.; Gong, Y.; Dai, J.; Gong, A.; Han, X.; Yao, Y.; Wang, C.; Wang, Y.; Chen, Y.; Yan, C.; et al. Flexible, Solid-State, Ion-Conducting Membrane with 3D Garnet Nanofiber Networks for Lithium Batteries. *Proc. Natl. Acad. Sci. U. S. A.* **2016**, *113*, 7094−7099.
(34) Luo, W.; Gong, Y.; Zhu, Y.; Li, Y.; Yao, Y.; Zhang, Y.; Fu, K. K.; Pastel, G.; Lin, C.-F.; Mo, Y.; et al. Reducing Interfacial Resistance between Garnet-Structured Solid-State Electrolyte and Li-Metal Anode by a Germanium Layer. *Adv. Mater.* **2017**, *29*, 1606042.

DOI: 10.1021/acs.chemmater.8b01713
Chem. Mater. 2018, 30, 6259−6276

(35) Fu, K. K.; Gong, Y.; Liu, B.; Zhu, Y.; Xu, S.; Yao, Y.; Luo, W.; Wang, C.; Lacey, S. D.; Dai, J.; et al. Toward Garnet Electrolyte–based Li Metal Batteries: An Ultrathin, Highly Effective, Artificial Solid-State Electrolyte/metallic Li Interface. *Sci. Adv.* **2017**, *3*, e1601659.
(36) Sharafi, A.; Yu, S.; Naguib, M.; Lee, M.; Ma, C.; Meyer, H. M.; Nanda, J.; Chi, M.; Siegel, D. J.; Sakamoto, J. Impact of Air Exposure and Surface Chemistry on Li–Li 7 La 3 Zr 2 O 12 Interfacial Resistance. *J. Mater. Chem. A* **2017**, *5*, 13475–13487.
(37) Sharafi, A.; Kazyak, E.; Davis, A. L.; Yu, S.; Thompson, T.; Siegel, D. J.; Dasgupta, N. P.; Sakamoto, J. Surface Chemistry Mechanism of Ultra-Low Interfacial Resistance in the Solid-State Electrolyte Li 7 La 3 Zr 2 O 12. *Chem. Mater.* **2017**, *29*, 7961–7968.
(38) Han, X.; Gong, Y.; Fu, K.; He, X.; Hitz, G. T.; Dai, J.; Pearse, A.; Liu, B.; Wang, H.; Rubloff, G.; et al. Negating Interfacial Impedance in Garnet-Based Solid-State Li Metal Batteries. *Nat. Mater.* **2016**, *16*, 572–579.
(39) Cheng, L.; Crumlin, E. J.; Chen, W.; Qiao, R.; Hou, H.; Franz Lux, S.; Zorba, V.; Russo, R.; Kostecki, R.; Liu, Z.; et al. The Origin of High Electrolyte–electrode Interfacial Resistances in Lithium Cells Containing Garnet Type Solid Electrolytes. *Phys. Chem. Chem. Phys.* **2014**, *16*, 18294–18300.
(40) Wang, C.; Gong, Y.; Liu, B.; Fu, K.; Yao, Y.; Hitz, E.; Li, Y.; Dai, J.; Xu, S.; Luo, W.; et al. Conformal, Nanoscale ZnO Surface Modification of Garnet-Based Solid-State Electrolyte for Lithium Metal Anodes. *Nano Lett.* **2017**, *17*, 565–571.
(41) Fu, K.; Gong, Y.; Dai, J.; Gong, A.; Han, X.; Yao, Y.; Wang, C.; Wang, Y.; Chen, Y.; Yan, C.; et al. Flexible, Solid-State, Ion-Conducting Membrane with 3D Garnet Nanofiber Networks for Lithium Batteries. *Proc. Natl. Acad. Sci. U. S. A.* **2016**, *113*, 201600422.
(42) Cheng, L.; Chen, W.; Kunz, M.; Persson, K.; Tamura, N.; Chen, G.; Doeff, M. Effect of Surface Microstructure on Electrochemical Performance of Garnet Solid Electrolytes. *ACS Appl. Mater. Interfaces* **2015**, *7*, 2073–2081.
(43) Kumar, P. J.; Nishimura, K.; Senna, M.; Düvel, A.; Heitjans, P.; Kawaguchi, T.; Sakamoto, N.; Wakiya, N.; Suzuki, H. A Novel Low-Temperature Solid-State Route for Nanostructured Cubic Garnet Li 7 La 3 Zr 2 O 12 and Its Application to Li-Ion Battery. *RSC Adv.* **2016**, *6*, 62656–62667.
(44) Wu, J.-F.; Pang, W. K.; Peterson, V. K.; Wei, L.; Guo, X. Garnet-Type Fast Li-Ion Conductors with High Ionic Conductivities for All-Solid-State Batteries. *ACS Appl. Mater. Interfaces* **2017**, *9*, 12461–12468.
(45) Wang, Z.; Santhanagopalan, D.; Zhang, W.; Wang, F.; Xin, H. L.; He, K.; Li, J.; Dudney, N.; Meng, Y. S. In Situ STEM-EELS Observation of Nanoscale Interfacial Phenomena in All-Solid-State Batteries. *Nano Lett.* **2016**, *16*, 3760–3767.
(46) Liu, T.; Ren, Y.; Shen, Y.; Zhao, S.-X.; Lin, Y.; Nan, C.-W. Achieving High Capacity in Bulk-Type Solid-State Lithium Ion Battery Based on Li6.75La3Zr1.75Ta0.25O12 Electrolyte: Interfacial Resistance. *J. Power Sources* **2016**, *324*, 349–357.
(47) Park, K.; Yu, B.-C.; Jung, J.-W.; Li, Y.; Zhou, W.; Gao, H.; Son, S.; Goodenough, J. B. Electrochemical Nature of the Cathode Interface for a Solid-State Lithium-Ion Battery: Interface between LiCoO 2 and Garnet-Li 7 La 3 Zr 2 O 12. *Chem. Mater.* **2016**, *28*, 8051–8059.
(48) Kotobuki, M.; Kanamura, K.; Sato, Y.; Yoshida, T. Fabrication of All-Solid-State Lithium Battery with Lithium Metal Anode Using Al2O3-Added Li7La3Zr 2O12 Solid Electrolyte. *J. Power Sources* **2011**, *196*, 7750–7754.
(49) Kim, K. H.; Iriyama, Y.; Yamamoto, K.; Kumazaki, S.; Asaka, T.; Tanabe, K.; Fisher, C. A. J.; Hirayama, T.; Murugan, R.; Ogumi, Z. Characterization of the Interface between LiCoO2 and Li 7La3Zr2O12 in an All-Solid-State Rechargeable Lithium Battery. *J. Power Sources* **2011**, *196*, 764–767.
(50) Uhlenbruck, S.; Dornseiffer, J.; Lobe, S.; Dellen, C.; Tsai, C.-L.; Gotzen, B.; Sebold, D.; Finsterbusch, M.; Guillon, O. Cathode-Electrolyte Material Interactions during Manufacturing of Inorganic Solid-State Lithium Batteries. *J. Electroceram.* **2017**, *38*, 197–206.
(51) Ohta, S.; Kobayashi, T.; Seki, J.; Asaoka, T. Electrochemical Performance of an All-Solid-State Lithium Ion Battery with Garnet-Type Oxide Electrolyte. *J. Power Sources* **2012**, *202*, 332–335.
(52) Ohta, S.; Seki, J.; Yagi, Y.; Kihira, Y.; Tani, T.; Asaoka, T. Co-Sinterable Lithium Garnet-Type Oxide Electrolyte with Cathode for All-Solid-State Lithium Ion Battery. *J. Power Sources* **2014**, *265*, 40–44.
(53) Zhou, W.; Wang, S.; Li, Y.; Xin, S.; Manthiram, A.; Goodenough, J. B. Plating a Dendrite-Free Lithium Anode with a Polymer/Ceramic/Polymer Sandwich Electrolyte. *J. Am. Chem. Soc.* **2016**, *138*, 9385–9388.
(54) Wang, C.; Yang, Y.; Liu, X.; Zhong, H.; Xu, H.; Xu, Z.; Shao, H.; Ding, F. Suppression of Lithium Dendrite Formation by Using LAGP-PEO (LiTFSI) Composite Solid Electrolyte and Lithium Metal Anode Modified by PEO (LiTFSI) in All-Solid-State Lithium Batteries. *ACS Appl. Mater. Interfaces* **2017**, *9*, 13694–13702.
(55) Liu, B.; Gong, Y.; Fu, K.; Han, X.; Yao, Y.; Pastel, G.; Yang, C.; Xie, H.; Wachsman, E. D.; Hu, L. Garnet Solid Electrolyte Protected Li-Metal Batteries. *ACS Appl. Mater. Interfaces* **2017**, *9*, 18809–18815.
(56) Miara, L.; Windmüller, A.; Tsai, C.-L.; Richards, W. D.; Ma, Q.; Uhlenbruck, S.; Guillon, O.; Ceder, G. About the Compatibility between High Voltage Spinel Cathode Materials and Solid Oxide Electrolytes as a Function of Temperature. *ACS Appl. Mater. Interfaces* **2016**, *8*, 26842–26850.
(57) Ren, Y.; Liu, T.; Shen, Y.; Lin, Y.; Nan, C.-W. Chemical Compatibility between Garnet-like Solid State Electrolyte Li6.75-La3Zr1.75Ta0.25O12 and Major Commercial Lithium Battery Cathode Materials. *J. Mater.* **2016**, *2*, 256–264.
(58) Miara, L. J.; Richards, W. D.; Wang, Y. E.; Ceder, G. First-Principles Studies on Cation Dopants and Electrolytelcathode Interphases for Lithium Garnets. *Chem. Mater.* **2015**, *27*, 4040–4047.
(59) Richards, W. D.; Miara, L. J.; Wang, Y.; Kim, J. C.; Ceder, G. Interface Stability in Solid-State Batteries. *Chem. Mater.* **2016**, *28*, 266–273.
(60) Zhu, Y.; He, X.; Mo, Y. First Principles Study on Electrochemical and Chemical Stability of Solid Electrolyte–electrode Interfaces in All-Solid-State Li-Ion Batteries. *J. Mater. Chem. A* **2016**, *4*, 3253–3266.
(61) Rubio-Zuazo, J.; Castro, G. R. Information Depth Determination for Hard X-Ray Photoelectron Spectroscopy up to 15 keV Photoelectron Kinetic Energy. *Surf. Interface Anal.* **2008**, *40*, 1438–1443.
(62) Claessen, R.; Sing, M.; Paul, M.; Berner, G.; Wetscherek, A.; Müller, A.; Drube, W. Hard X-Ray Photoelectron Spectroscopy of Oxide Hybrid and Heterostructures: A New Method for the Study of Buried Interfaces. *New J. Phys.* **2009**, *11*, 125007.
(63) Ren, Y.; Liu, T.; Shen, Y.; Lin, Y.; Nan, C.-W. Chemical Compatibility between Garnet-like Solid State Electrolyte Li6.75-La3Zr1.75Ta0.25O12 and Major Commercial Lithium Battery Cathode Materials. *J. Mater.* **2016**, *2*, 256–264.
(64) Lin, F.; Markus, I. M.; Doeff, M. M.; Xin, H. L. Chemical and Structural Stability of Lithium-Ion Battery Electrode Materials under Electron Beam. *Sci. Rep.* **2015**, *4*, 5694.
(65) Yao, K. P. C.; Kwabi, D. G.; Quinlan, R. A.; Mansour, A. N.; Grimaud, A.; Lee, Y.-L.; Lu, Y.-C.; Shao-Horn, Y. Thermal Stability of Li2O2 and Li2O for Li-Air Batteries: In Situ XRD and XPS Studies. *J. Electrochem. Soc.* **2013**, *160*, A824–A831.
(66) Xia, W.; Xu, B.; Duan, H.; Guo, Y.; Kang, H.; Li, H.; Liu, H. Ionic Conductivity and Air Stability of Al-Doped Li 7 La 3 Zr 2 O 12 Sintered in Alumina and Pt Crucibles. *ACS Appl. Mater. Interfaces* **2016**, *8*, 5335–5342.
(67) Tsvetkov, N.; Lu, Q.; Sun, L.; Crumlin, E. J.; Yildiz, B. Improved Chemical and Electrochemical Stability of Perovskite Oxides with Less Reducible Cations at the Surface. *Nat. Mater.* **2016**, *15*, 1010–1016.
(68) Hu, Z.; Grazioli, C.; Knupfer, M.; Golden, M. S.; Fink, J.; Mahadevan, P.; Kumar, A.; Ray, S.; Sarma, D. D.; Warda, S. A.; et al.

DOI: 10.1021/acs.chemmater.8b01713
Chem. Mater. 2018, 30, 6259–6276

Difference in Spin State and Covalence between La1-xSrxCoO3 and La2-xSrxLi0.5Co0.5O4. *J. Alloys Compd.* **2002**, *343*, 5−13.
(69) Chen, C.-H.; Hwang, B.-J.; Chen, C.-Y.; Hu, S.-K.; Chen, J.-M.; Sheu, H.-S.; Lee, J.-F. Soft X-Ray Absorption Spectroscopy Studies on the Chemically Delithiated Commercial LiCoO2 Cathode Material. *J. Power Sources* **2007**, *174*, 938−943.
(70) Liao, C.-L.; Fung, K.-Z. Lithium Cobalt Oxide Cathode Film Prepared by Rf Sputtering. *J. Power Sources* **2004**, *128*, 263−269.
(71) Haas, O.; Struis, R. P. W. J.; McBreen, J. Synchrotron X-Ray Absorption of LaCoO3 Perovskite. *J. Solid State Chem.* **2004**, *177*, 1000−1010.
(72) Kuzmin, A.; Efimov, V.; Efimova, E.; Sikolenko, V.; Pascarelli, S.; Troyanchuk, I. O. Interpretation of the Co K-Edge EXAFS in LaCoO3 Using Molecular Dynamics Simulations. *Solid State Ionics* **2011**, *188*, 21−24.
(73) Risch, M.; Grimaud, A.; May, K. J.; Stoerzinger, K. A.; Chen, T. J.; Mansour, A. N.; Shao-Horn, Y. Structural Changes of Cobalt-Based Perovskites upon Water Oxidation Investigated by EXAFS. *J. Phys. Chem. C* **2013**, *117*, 8628−8635.
(74) Jorissen, K.; Rehr, J. J. New Developments in FEFF: FEFF9 and JFEFF. *J. Phys.: Conf. Ser.* **2013**, *430*, 12001.
(75) Rehr, J. J.; Kas, J. J.; Vila, F. D.; Prange, M. P.; Jorissen, K. Parameter-Free Calculations of X-Ray Spectra with FEFF9. *Phys. Chem. Chem. Phys.* **2010**, *12*, 5503.
(76) Wenzel, S.; Weber, D. A.; Leichtweiss, T.; Busche, M. R.; Sann, J.; Janek, J. Interphase Formation and Degradation of Charge Transfer Kinetics between a Lithium Metal Anode and Highly Crystalline Li7P3S11 Solid Electrolyte. *Solid State Ionics* **2016**, *286*, 24−33.
(77) Buschmann, H.; Dölle, J.; Berendts, S.; Kuhn, A.; Bottke, P.; Wilkening, M.; Heitjans, P.; Senyshyn, A.; Ehrenberg, H.; Lotnyk, A.; et al. Structure and Dynamics of the Fast Lithium Ion Conductor "Li7La3Zr2O12. *Phys. Chem. Chem. Phys.* **2011**, *13*, 19378.
(78) Bernuy-Lopez, C.; Manalastas, W.; Lopez del Amo, J. M.; Aguadero, A.; Aguesse, F.; Kilner, J. A. Atmosphere Controlled Processing of Ga-Substituted Garnets for High Li-Ion Conductivity Ceramics. *Chem. Mater.* **2014**, *26*, 3610−3617.
(79) Wagner, R.; Redhammer, G. J.; Rettenwander, D.; Tippelt, G.; Welzl, A.; Taibl, S.; Fleig, J.; Franz, A.; Lottermoser, W.; Amthauer, G. Fast Li-Ion-Conducting Garnet-Related Li 7−3 X Fe X La 3 Zr 2 O 12 with Uncommon I $\bar{4}$3 D Structure. *Chem. Mater.* **2016**, *28*, 5943−5951.
(80) Irvine, J. T. S.; Sinclair, D. C.; West, A. R. Electroceramics: Characterization by Impedance Spectroscopy. *Adv. Mater.* **1990**, *2*, 132−138.
(81) Kato, T.; Hamanaka, T.; Yamamoto, K.; Hirayama, T.; Sagane, F.; Motoyama, M.; Iriyama, Y. In-Situ Li 7 La 3 Zr 2 O 12 /LiCoO 2 Interface Modification for Advanced All-Solid-State Battery. *J. Power Sources* **2014**, *260*, 292−298.
(82) Clements, R. J. *Structure and Bonding in Lanthanide Zirconates*; Elsevier, 2011.
(83) Imamura, M.; Matsubayashi, N.; Shimada, H. Catalytically Active Oxygen Species in La 1-X Sr X CoO 3-δ Studied by XPS and XAFS Spectroscopy. *J. Phys. Chem. B* **2000**, *104*, 7348−7353.
(84) Merz, M.; Fuchs, D.; Assmann, A.; Uebe, S.; v. Löhneysen, H.; Nagel, P.; Schuppler, S. Spin and Orbital States in Single-Layered La2−xCaxCoO4 Studied by Doping- and Temperature-Dependent near-Edge X-Ray Absorption Fine Structure. *Phys. Rev. B: Condens. Matter Mater. Phys.* **2011**, *84*, 14436.
(85) ZHANG, Z. Electrochemical Properties of Room Temperature Ionic Liquids Incorporating BF4− and TFSI− Anions as Green Electrolytes. *Chin. Sci. Bull.* **2005**, *50*, 2005.
(86) Baek, S. W.; Lee, J. M.; Kim, T. Y.; Song, M. S.; Park, Y. Garnet Related Lithium Ion Conductor Processed by Spark Plasma Sintering for All Solid State Batteries. *J. Power Sources* **2014**, *249*, 197−206.
(87) Yamada, H.; Ito, T.; Hongahally Basappa, R. Sintering Mechanisms of High-Performance Garnet-Type Solid Electrolyte Densified by Spark Plasma Sintering. *Electrochim. Acta* **2016**, *222*, 648−656.
(88) Liu, B.; Fu, K.; Gong, Y.; Yang, C.; Yao, Y.; Wang, Y.; Wang, C.; Kuang, Y.; Pastel, G.; Xie, H.; et al. Rapid Thermal Annealing of Cathode-Garnet Interface toward Higherature Solid State Batteries. *Nano Lett.* **2017**, *17*, 4917−4923.
(89) Guo, J.; Guo, H.; Baker, A. L.; Lanagan, M. T.; Kupp, E. R.; Messing, G. L.; Randall, C. A. Cold Sintering: A Paradigm Shift for Processing and Integration of Ceramics. *Angew. Chem., Int. Ed.* **2016**, *55*, 11457−11461.
(90) Moses, A. W.; Flores, H. G. G.; Kim, J.-G.; Langell, M. A. Surface Properties of LiCoO2, LiNiO2 and LiNi1−xCoxO2. *Appl. Surf. Sci.* **2007**, *253*, 4782−4791.
(91) Grass, M. E.; Karlsson, P. G.; Aksoy, F.; Lundqvist, M.; Wannberg, B.; Mun, B. S.; Hussain, Z.; Liu, Z. New Ambient Pressure Photoemission Endstation at Advanced Light Source Beamline 9.3.2. *Rev. Sci. Instrum.* **2010**, *81*, 53106.
(92) Ravel, B.; Newville, M. ATHENA, ARTEMIS, HEPHAESTUS : Data Analysis for X-Ray Absorption Spectroscopy Using IFEFFIT. *J. Synchrotron Radiat.* **2005**, *12*, 537−541.
(93) Chater, R. J.; Smith, A. J.; Cooke, G. Simultaneous Detection of Positive and Negative Secondary Ions. *J. Vac. Sci. Technol., B: Nanotechnol. Microelectron.: Mater., Process., Meas., Phenom.* **2016**, *34*, 03H122.

DOI: 10.1021/acs.chemmater.8b01713
Chem. Mater. 2018, 30, 6259−6276

Supplementary Materials for "Structure, Chemistry, and Charge Transfer Resistance of the Interface between $Li_7La_3Zr_2O_{12}$ Electrolyte and $LiCoO_2$ Cathode"

Gulin Vardar[1,❖], William J. Bowman[1], Qiyang Lu[2], Jiayue Wang[1], Richard J. Chater[3], Ainara Aguadero[3], Rachel Seibert[4], Jeff Terry[4], Adrian Hunt[5], Iradwikanari Waluyo[5], Dillon D. Fong[6], Angelique Jarry[7,8], Ethan J. Crumlin[8], Sondra L. Hellstrom[9], Yet-Ming Chiang[2], Bilge Yildiz[1,2,*]

[1]Department of Nuclear Science and Engineering, Massachusetts Institute of Technology, Cambridge, Massachusetts 02139, USA

[2]Department of Materials Science and Engineering, Massachusetts Institute of Technology, Cambridge, Massachusetts 02139, USA

[3]Department of Materials, Imperial College of Science, London SW7 2AZ, UK

[4]Department of Physics, Illinois Institute of Technology, Chicago, Illinois 60616, USA

[5]National Synchrotron Light Source II, Brookhaven National Laboratory, Upton, New York 11973, USA

[6]Advanced Photon Source, Argonne National Laboratory, Lemont, Illinois 60439, USA

[7]Department of Chemistry and Biochemistry, University of Maryland, College Park, Maryland, 20742, USA

[8]Advanced Light Source, Lawrence Berkeley National Laboratory, Berkeley, California 94720, USA

[9]Bosch Research and Technology Center, Sunnyvale, California 94085, USA

❖Current Address: Department of Mechanical Engineering, Bogazici University, Istanbul, 34342 Turkey

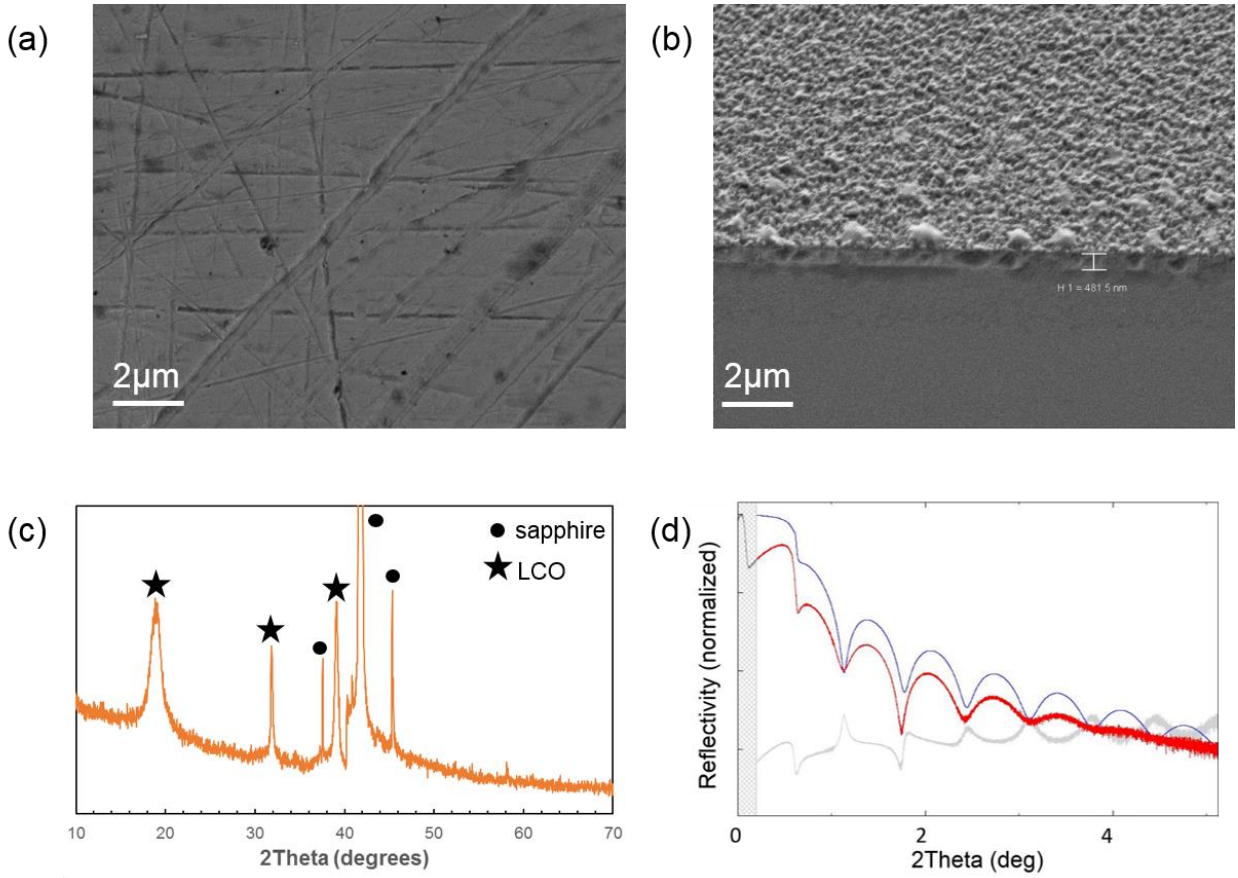

Figure S1. (a) Scanning electron microscopy image of polished LLZO surface. (b) Scanning electron microscopy image of 460 nm LCO deposition on single-crystal sapphire substrate. (c) X-ray diffraction spectra for 460 nm LCO deposition on single-crystal sapphire substrate. (d) X-ray reflectivity measurements for 10 nm LCO deposition on single-crystal sapphire substrate. The simulation for 10 nm LCO deposition on sapphire is plotted in red.

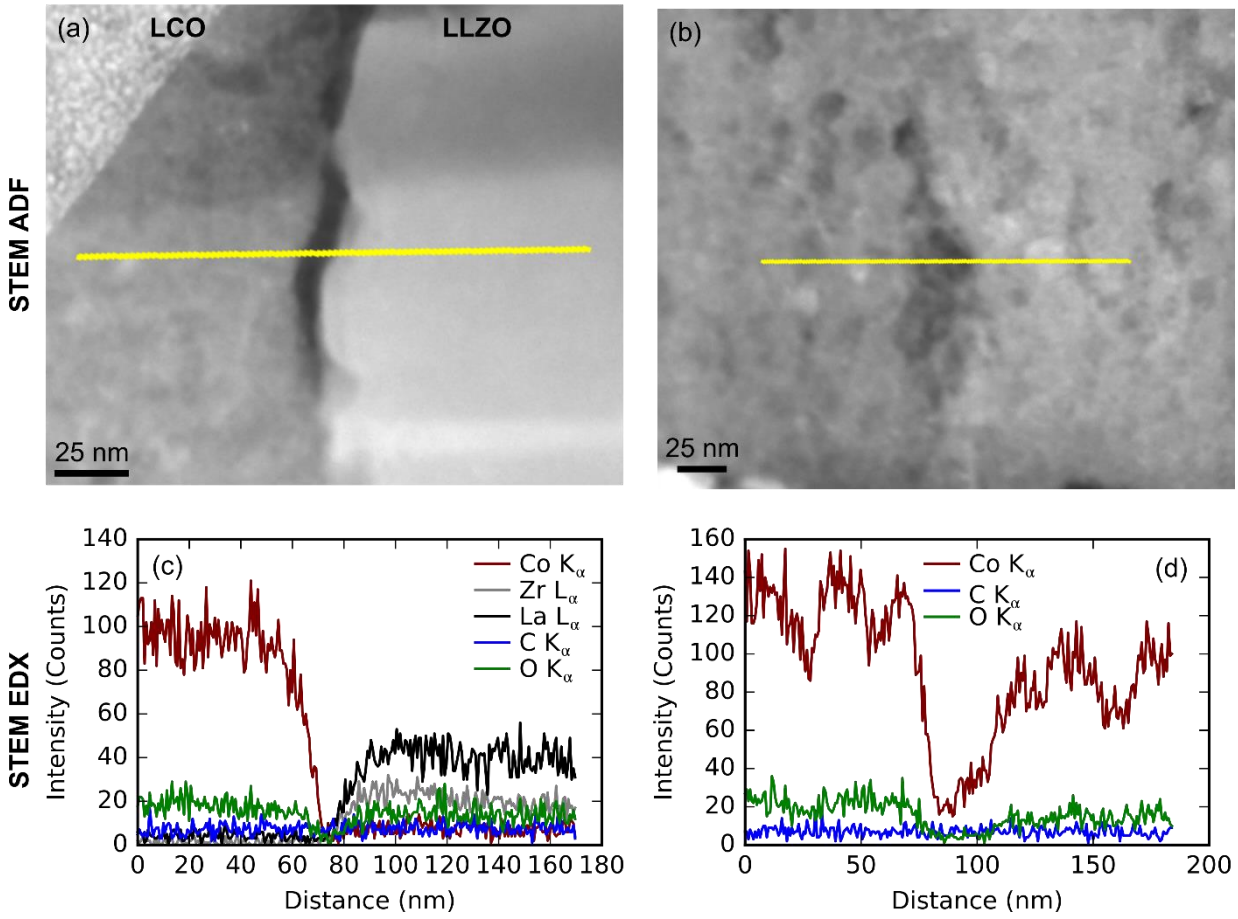

Figure S2. STEM EDX analysis of voids observed at the LCO-LLZO interface and in the LCO phase after 500 °C annealing. STEM ADF images of the LCO-LLZO interface (a) and LCO phase (b) with EDX line scan paths indicated with horizontal lines. (c,d) EDX signal intensity profiles corresponding to images (a) and (b), respectively.

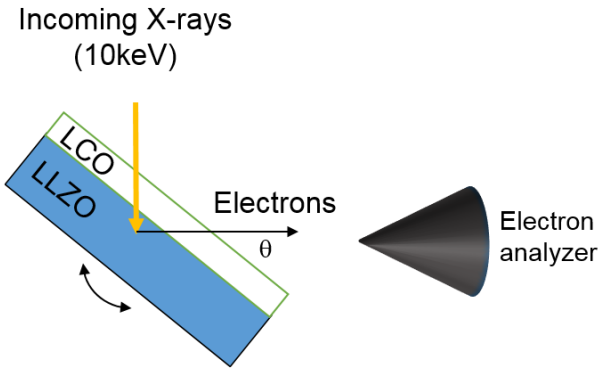

Figure S3. Configuration of the hard x-ray photoelectron spectroscopy setup. Emission angle is labeled as θ.

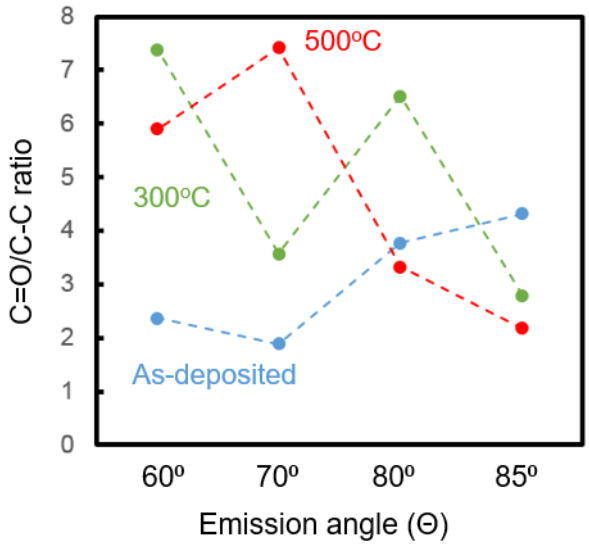

Figure S4. C=O/C-C ratio obtained by C 1s hard X-ray photoelectron spectroscopy as a function of emission angle for the LCO|LLZO samples, with a 20 nm deposited LCO layer, in the as-deposited state, and after annealing at 300°C and 500°C.

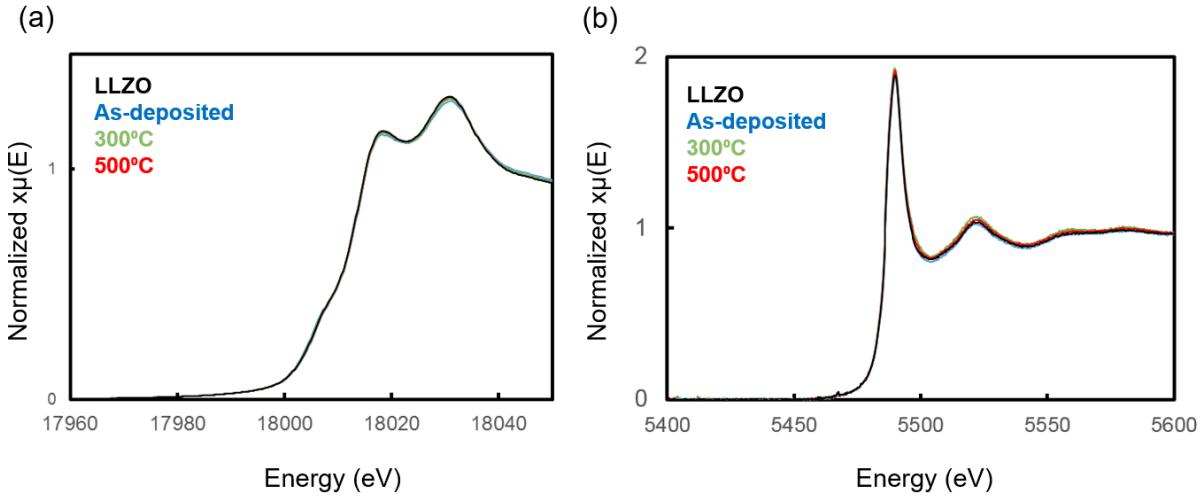

Figure S5. (a) Zr K-edge and (b) La L_3-edge X-ray absorption spectroscopy data for LLZO, and LCO|LLZO samples, with 460 nm deposited LCO layer in the as-deposited state, and after annealing at 300°C and 500°C.

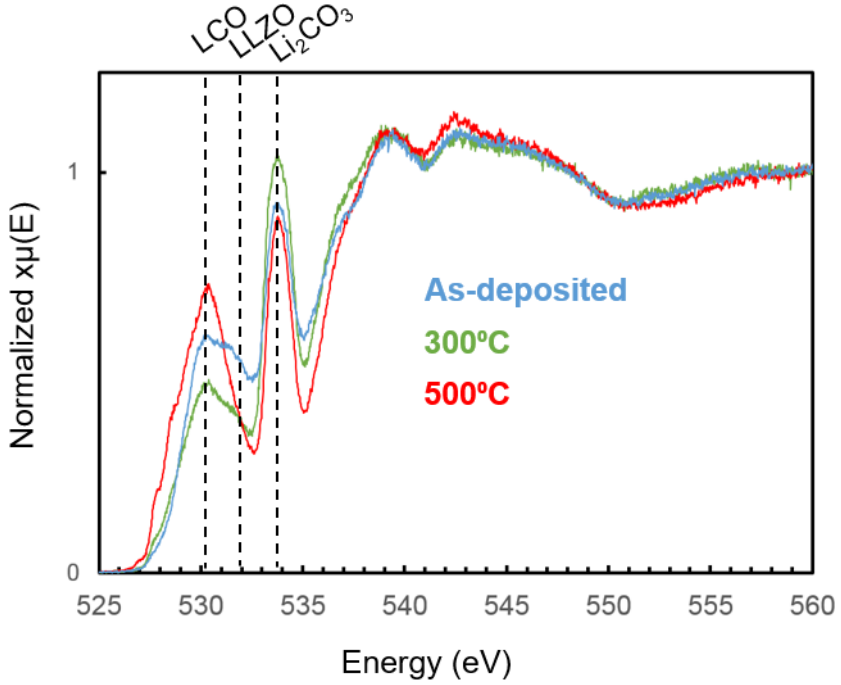

Figure S6. Normalized O K-edge X-ray absorption spectroscopy data for LCO|LLZO samples, with 460 nm deposited LCO layer in the as-deposited state, and after annealing at 300ºC and 500ºC.

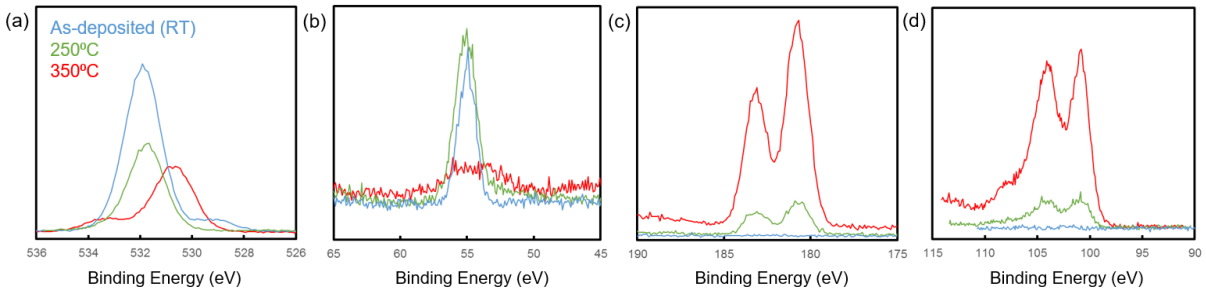

Figure S7. (a) O 1s, (b) Li 1s, (c) Zr 3d, (d) La 4d X-ray photoelectron spectroscopy spectra for a LLZO pellet measured in situ at room temperature, 250^{0}C and 350^{0}C in 30 mTorr pure O_2.

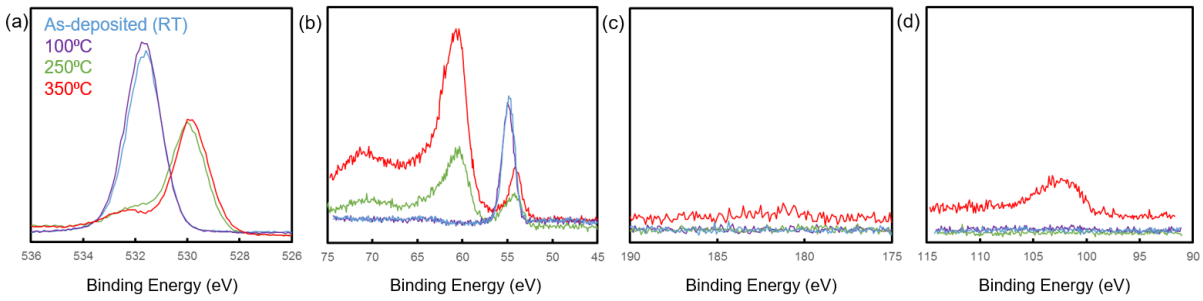

Figure S8. (a) O 1s, (b) Co 3d and Li 1s, (c) Zr 3d, (d) La 4d X-ray photoelectron spectroscopy spectra for a LCO|LLZO sample, with a 20 nm deposited LCO layer, measured in situ at room temperature, 100^{0}C, 250^{0}C, and 350^{0}C in 30 mTorr of pure O_2.

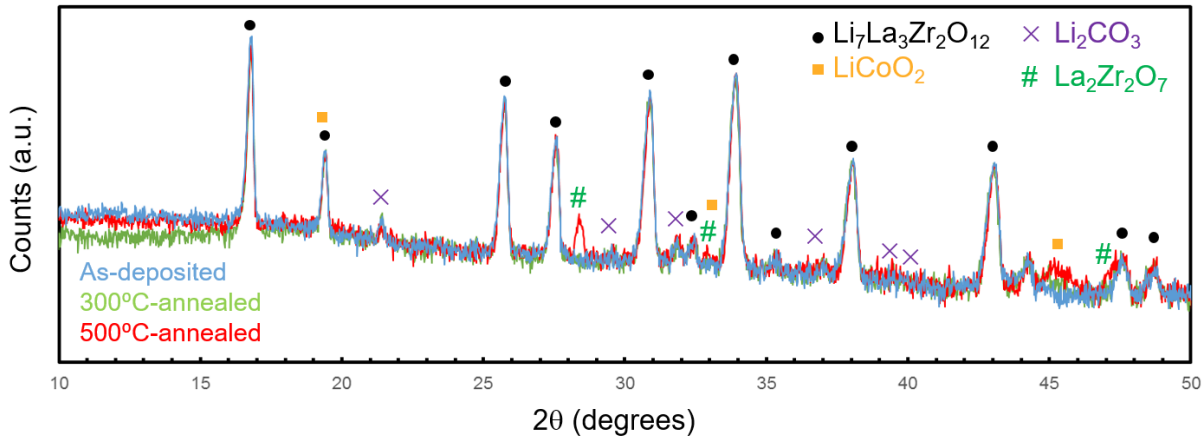

Figure S9. X-ray diffraction spectra for LCO|LLZO samples, with 460 nm deposited LCO layer in the as-deposited state, and after annealing at 300ºC and 500ºC.

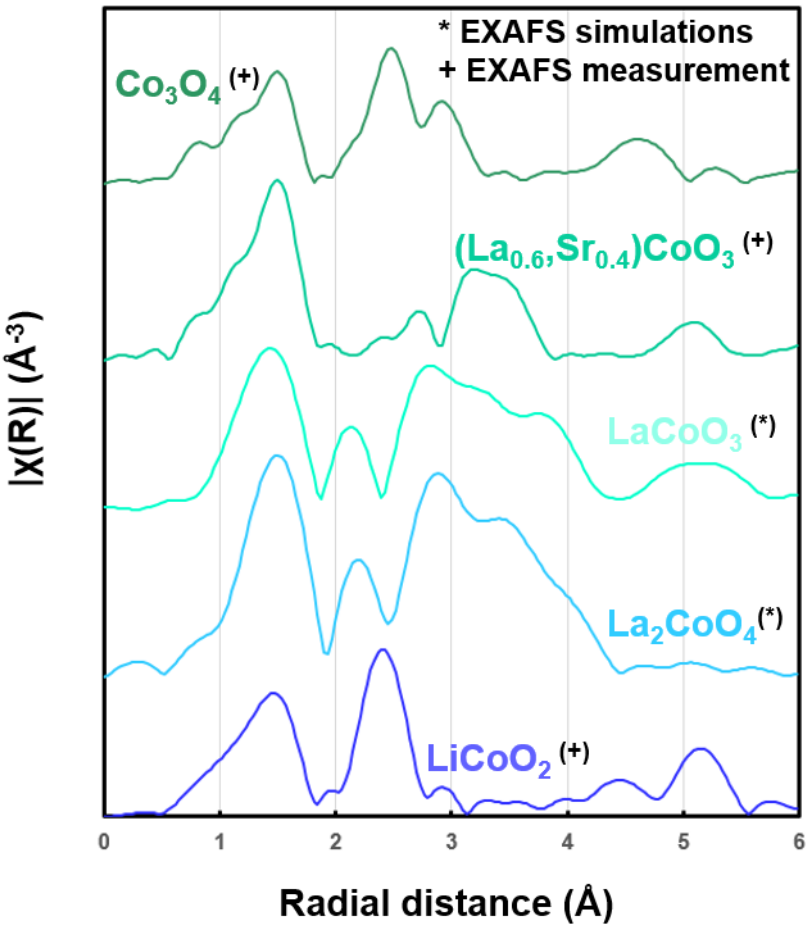

Figure S10. Fourier-transform of Co extended X-ray absorption fine structure spectra for measured LCO, $La_{0.6}Sr_{0.4}CoO_3$ and Co_3O_4 reference samples and calculated extended X-ray absorption fine structure spectra for $LaCoO_3$ and La_2CoO_4.

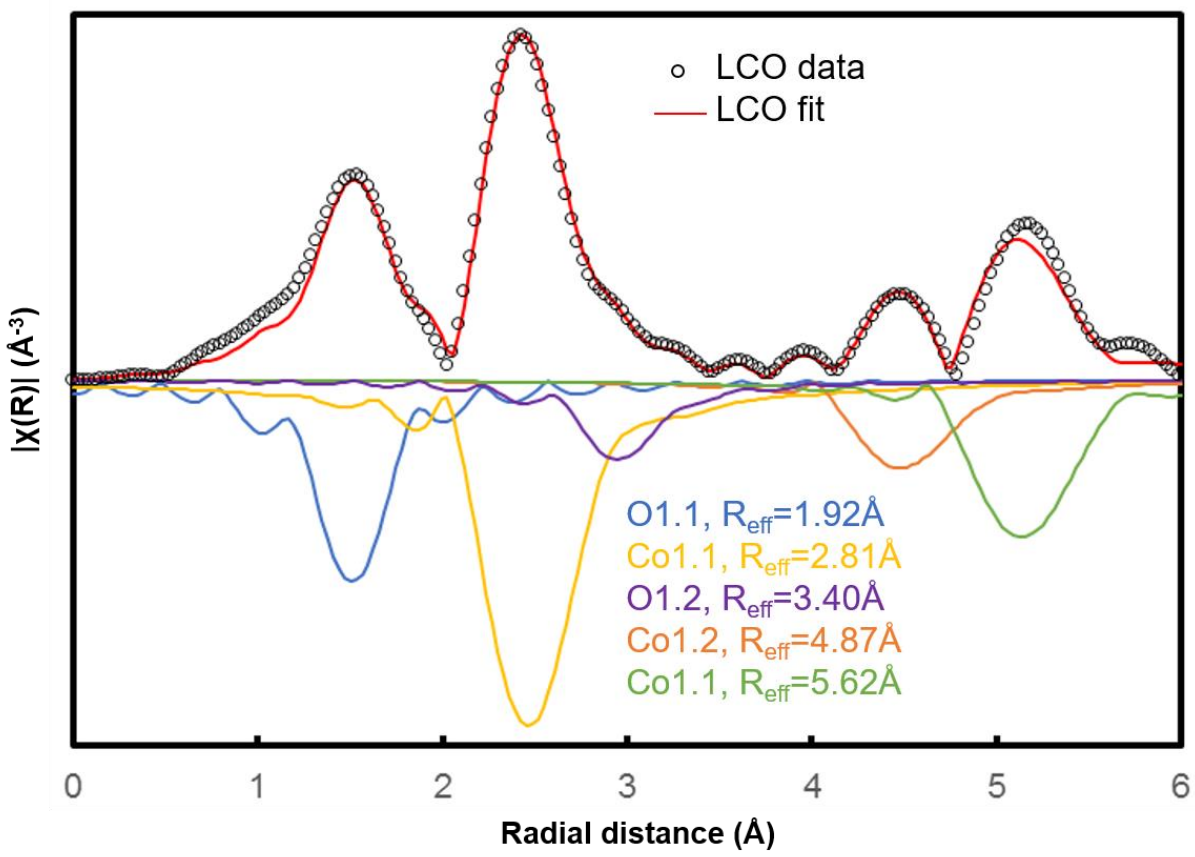

Figure S11. The magnitude of the Fourier-transformed k^2-weighted data and the fit for the LCO reference sample are shown along with the fitting paths used in the model (reflected about the x-axis for clarity).

Table S1. Fitting results for the fit of the LCO Co EXAFS data. A single value of E_0 was used for all paths, the best fit was -3.21 ± 0.79 eV. Uncertainties determined by inversion of the covariance matrix.

Path	$R_{perfectcrystal}$ (Å)	$R_{measured}$ (Å)	σ^2 (Å^2)	N
O 1.1	1.92	1.92 ± 0.01	0.0019 ± 0.0011	3.48 ± 0.39
Co 1.1	2.81	2.83 ± 0.01	0.0025 ± 0.0008	4.03 ± 0.52
O 1.2	3.40	3.41 ± 0.10	0.0009 ± 0.0002	7.54 ± 4.84
Co 1.2	4.87	4.93 ± 0.09	0.0065 ± 0.0045	10.27 ± 3.96
Co 1.1	5.62	5.60 ± 0.05	0.0001 ± 0.0002	2.05 ± 0.89

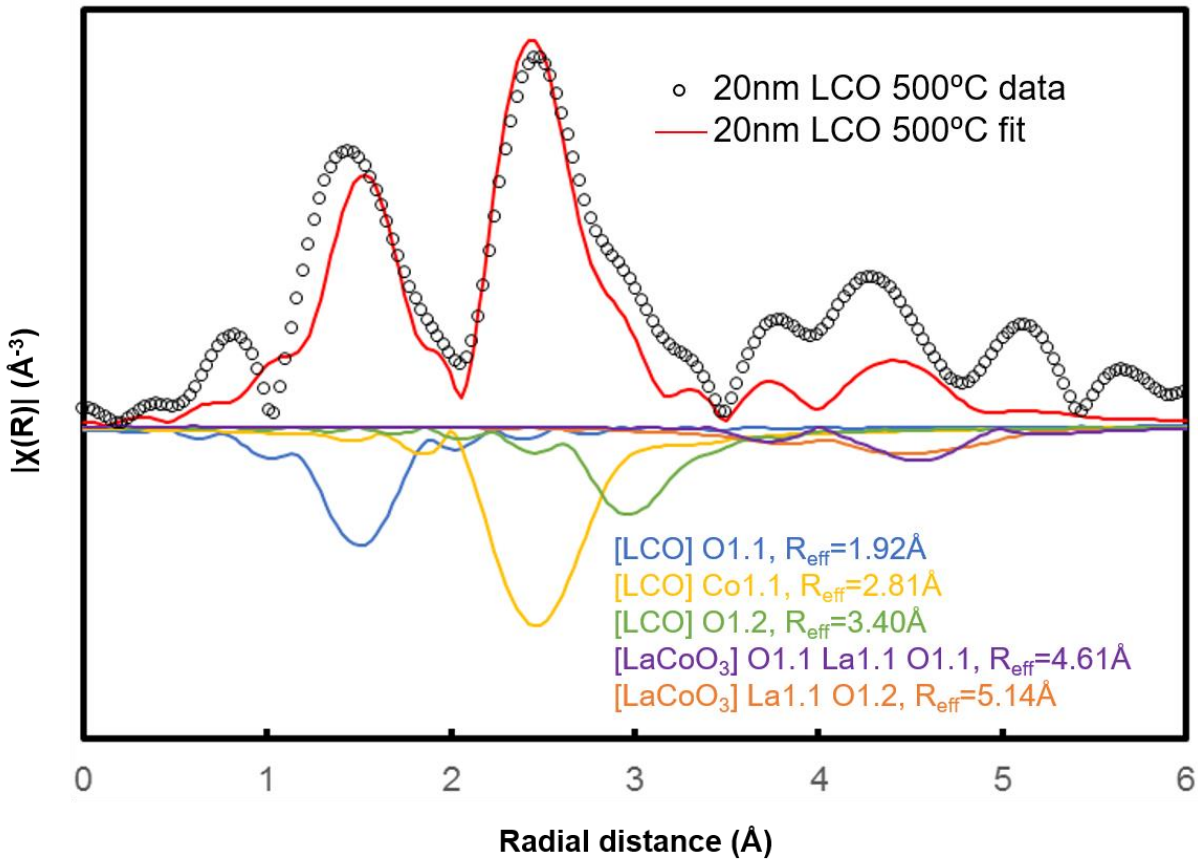

Figure S12. The magnitude of the Fourier-transformed k^2-weighted data and the fit for the 20 nm LCO sample after annealing at 500°C are shown along with the fitting paths used in the model (reflected about the x-axis for clarity).

Table S2 Fitting results for the fit of the LCO Co EXAFS data. A single value of E_0 was used for all paths, the best fit was -5.31 ± 3.59 eV. Uncertainties determined by inversion of the covariance matrix.

Path	$R_{perfectcrystal}$ (Å)	$R_{measured}$ (Å)	σ^2 (Å^2)
[LCO] O 1.1	1.92	1.90 ± 0.04	0.0015 ± 0.0036
[LCO] Co 1.1	2.81	2.82 ± 0.06	0.0029 ± 0.0031
[LCO] O 1.2	3.40	3.44 ± 0.44	0.0001 ± 0.0001
[$LaCoO_3$] O1.1 La 1.1 O 1.1	4.61	4.49 ± 0.20	0.0004 ± 0.0015
[$LaCoO_3$] La 1.1 O 1.2	5.14	5.10 ± 0.28	0.0001 ± 0.0290

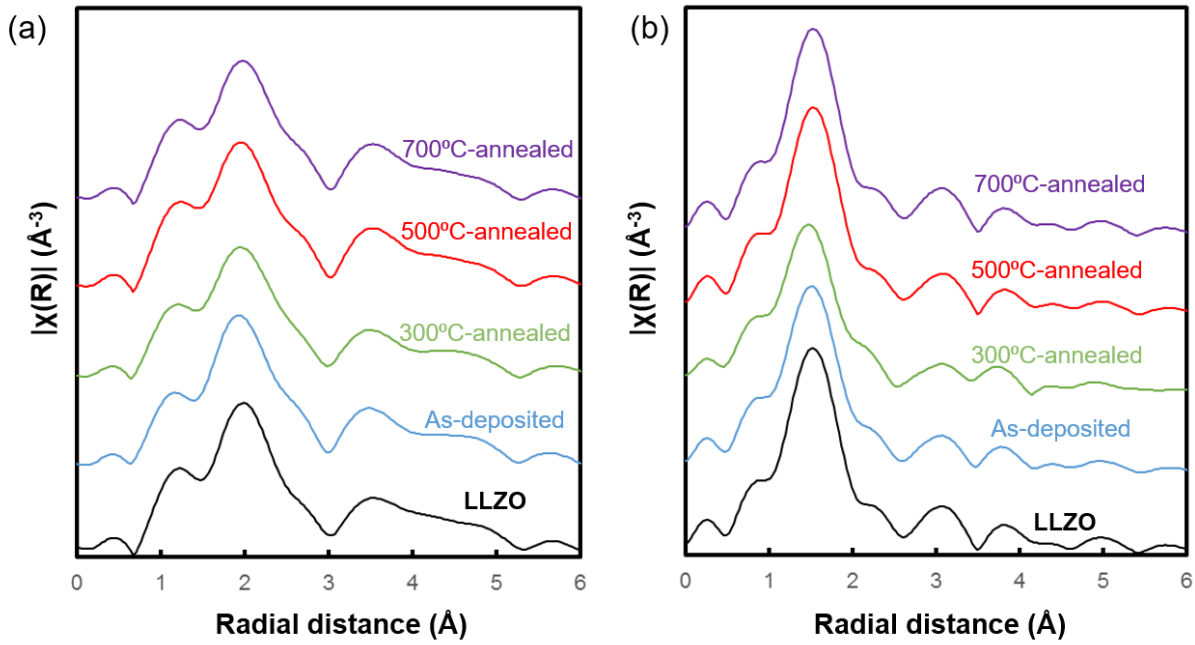

Figure S13 Fourier-transform of (a) La L_3-edge and (b) Zr K-edge extended X-ray absorption fine structure spectra for LLZO reference sample, and LCO|LLZO samples, with a 460 nm deposited LCO layer, in the as-deposited state, and after annealing at 300ºC, 500ºC, and 700ºC.

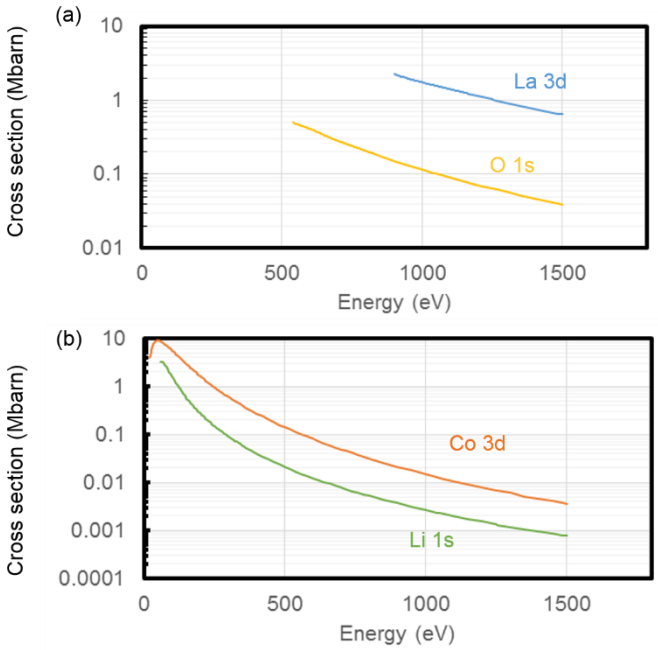

Figure S14 Photoionization cross sections for (a) La 3d and O 1s and (b) Co 3d and Li 1s.

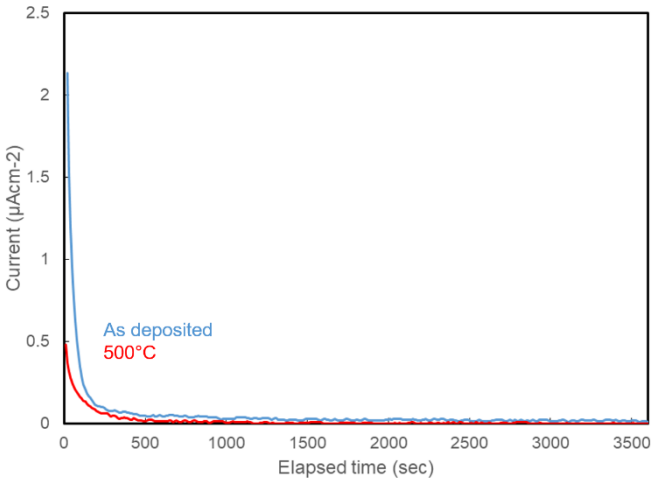

Figure S15. Current vs. time data during 3V potentiostatic hold (1 hour) for LCO|LLZO|LZO symmetric cells in the as-deposited state and after annealing at 500°C. For the as-deposited structure, integration of the current vs. time suggests that a ~1nm thick Li metal was plated on the +3V-side of the structure (assuming all of the current was spent on Li transfer).

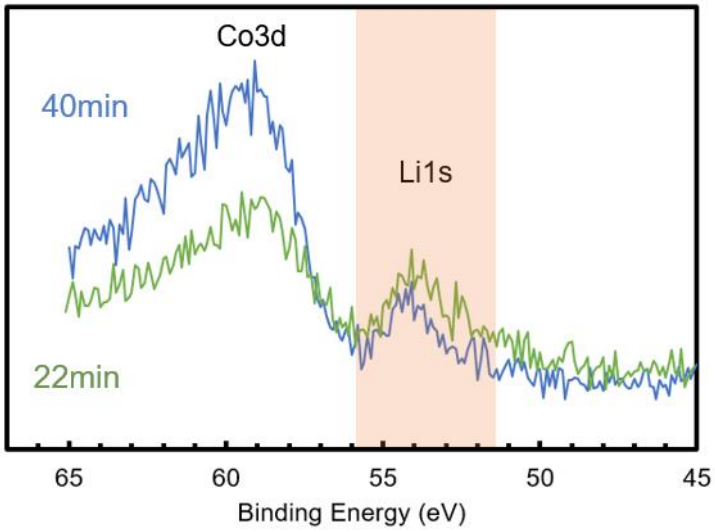

Figure S16. Li 1s and Co 3d x-ray photoelectron spectra for a symmetric LCO|LLZO|LCO structure after a 3V potentiostatic hold, taken after 22 min (green) and 40 min (blue) of depth profiling. The 22 min corresponds to the peak of the Li composition profile on the left-side of the cell in Figure 12(a), while the 40 min corresponds to the LCO region. The relative binding energy shift of the Li 1s peak after 22 minutes of sputtering indicates metallic lithium,[76] consistent with Li metal plating upon +3 V of potentiostatic hold.

Explanation of the potentiostatic-hold experiment using the LCO|LLZO|LCO symmetric cell

The experiment in Figure 12 is a two-electrode configuration. The working electrode is at the right LCO, and the counter *and* the reference electrodes together are at the left LCO layer. To start with OCV=0V, and both the left and the right LCO electrodes are at 3.9 V vs. Li/Li^+. Please see Table 3 below for the progression of voltages on both sides of the cell upon potentiostatic hold. When we apply 3V at the right LCO with respect to the left LCO, the right LCO potential rises to 6.9V vs. Li/Li^+. In order to take the current, Li starts delithiating from the right LCO, and shifts the right LCO electrode voltage to 4V (stable delithiation) and puts the excess Li on the left LCO side. And based on thermodynamics, this should shift the reference and counter electrode at the left LCO to 1V. It is possible here that we have a reductive decomposition of the left LCO phase to Li_2O and Co metal. However, we do not have evidence to this outcome. The Co 2p and Li 1s photoelectron intensities in the left LCO region is very similar to the non-polarized case (Figure 2a). In addition we have a ***separate*** Li peak to the left of the left-LCO electrode in Figure 12a. We have shown in S.I. Figure S16 that this separate Li peak has metallic Li character in Li 1s spectrum. And importantly, the Co 2p photoelectron spectrum clearly shows Co-oxide rather than Co metal, please see the new S.I. Figure S17 below demonstrating this. (Please note, there is *no* Co metal signature in the XPS data, even though such depth profiling by Ar sputtering can cause preferential sputtering of O atoms and cause reduction of the metal cations as an artifact). As a result, there is no Li_2O and no Co metal on the left LCO region. Therefore, we conclude that Li metal plating (shifting the voltage to 0V on the left) was *kinetically* (not thermodynamically) more favorable than the reductive decomposition. This means, the left-electrode potential is pinned to 0 V vs. Li/Li^+, then further decomposition of the LCO on that side is not an issue, and the right-LCO electrode voltage is pushed down to 3V. This would have been accompanied by oxidation of Li_xO_y on the right side. The Li_xO_y represent peroxide or super oxide species from the initial high oxidation voltage, which not only are able to oxidize Co^{3+} ($LiCoO_2$) to Co^{4+}(CoO_2) but also enough to oxide (O^{2-}) to O_2^{2-} and O_2. The oxidation of Li_xO_y process could happen in 3~3.5V region. The expected products are Li^+ (and it is moved to the left of the cell under the applied electric field), and O_2. O_2 loss is also apparent on the right-LCO zone – comparing the XPS profile in Figure 2a and Figure 12a(right side), we can see the latter has less O signal, consistent with evolving O_2. As a result, we end up with Li metal plating on left side, and Li^+ and O_2-loss (less oxygen in CoO_x,

more like Co_3O_4) on the right side, and Li^+ is drifted to the left side under electric potential gradient.

Table S1: Progression of voltages on both sides of the cell upon potentiostatic hold in Figure 12(a).

	Initial state	+3V at right LCO w.r.t. left LCO	Reference electrode (at the left LCO) drifts	Reference electrode (at the left LCO) drifts
Left LCO	3.9V vs Li/Li+	3.9V vs Li/Li+	1V vs Li/Li+	0V vs Li/Li+
	OCP	Initial over-lithiation	1st stable reaction, reductive decomposition of LiCoO2	Plating Li
Right LCO	3.9V vs Li/Li+	6.9V vs Li/Li+	4V vs Li/Li+	3V vs Li/Li+
	OCP	Initial oxidative decomposition of $LiCoO_2$	1st stable reaction, delithiation	Oxidation of Li_xO_y. Li^+ is drifted from right to left under electric field, and O_2 loss.

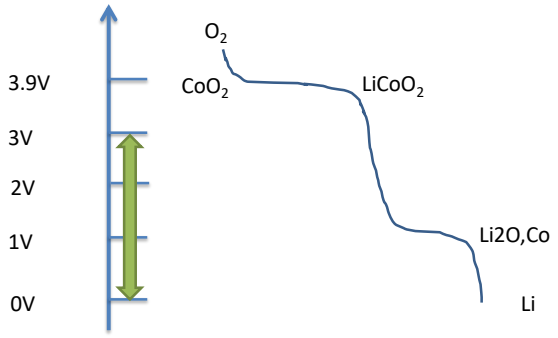

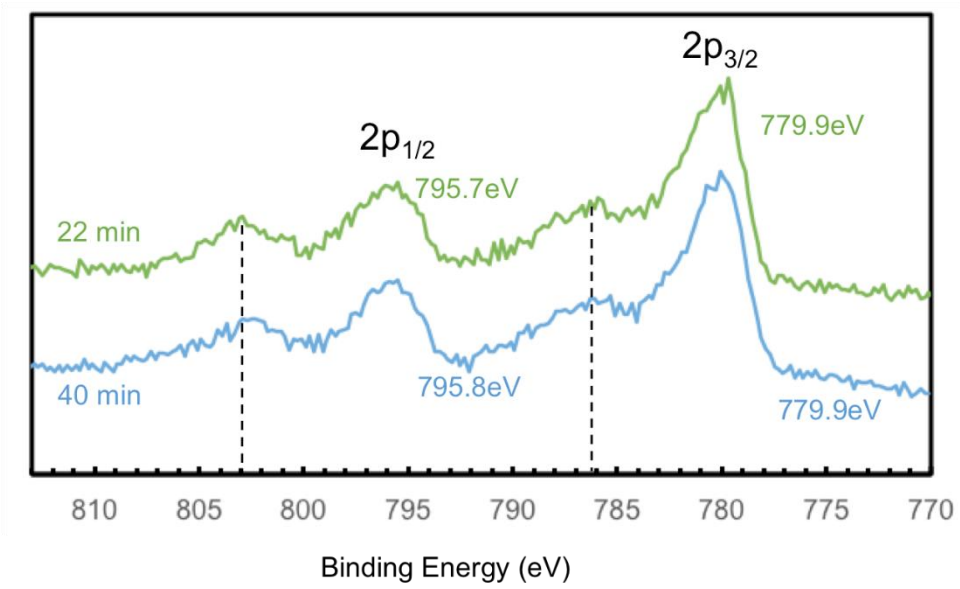

Figure S17: Co 2p spectra taken at the left LCO side upon potentiostatic polarization, from the 22 min and the 40 min positions. The peak position and the peak shape matches Co-oxide binding environment and not Co metal.

Co 2p photoelectron peaks for Co metal are 2 eV lower in binding energy than the 2p peaks for Co-oxide species.[95] Therefore, there would be a very obvious shift in the binding energies and peak shape if Co metal were to form on the left electrode. Furthermore, Co metal 2p specta exhibits no satellite peaks, which are clearly visible in our spectra typical of oxidized Co. Please note, it is not possible reliably to quantify the oxidation state of Co as 2^+ or 3^+ from Co 2p spectrum alone (they both have very complex sattelite peaks, making it impractical to quantify the oxidation state). But it is well established that the oxide and metal peaks of Co are clearly different, in binding energy and in shape, and our data matches the Co-oxide and not the Co metal.

The key point to note is that this experiment is clearly showing that Li was able to flow from the right to the left electrode (Figure 12 a) prior to annealing, and after annealing/sintering such a Li flowing process is no longer possible (Figure 12(b)) because of elemental interdiffusion and secondary phase formation similar to the profiles in Figure 2(c)). This result is complementary to the 8-fold increase in interface ASR shown in Figure 13.